Acta Geotechnica (2025) 20:1621–1642
https://doi.org/10.1007/s11440-024-02502-w

RESEARCH PAPER

THM-modelling benchmark initiative on the effects of temperature on the disposal of heat-generating radioactive waste in clay formations

Eric Simo[8,1] · **Christophe de Lesquen**[2] · **Rocio Paola Leon-Vargas**[1] · **Minh-ngoc Vu**[2] · **Simon Raude**[3] · **Ginger El Tabbal**[3] · **Arnaud Dizier**[4] · **Suresh Seetharam**[4] · **Asta Narkuniene**[5] · **Frédéric Collin**[6] · **Hangbiao Song**[6] · **Antonio Gens**[7] · **Fei Song**[7] · **Alexandru-Bogdan Tatomir**[10] · **Thomas Nagel**[8,9] · **Jörg Buchwald**[8,9]

Received: 22 December 2023 / Accepted: 1 December 2024 / Published online: 25 February 2025

Abstract

Understanding the thermo-hydro-mechanical (THM) behaviour of clay formations, which are being considered as potential hosts for the disposal of radioactive waste in Europe, is important for the feasibility and the safe disposal of heat-generating radioactive waste in deep geological clayey formations. To ensure the reliability of numerical models and tools used to predict the THM evolution of such systems over long periods of time, it is necessary to verify and validate these tools through benchmarking initiatives. As part of the joint European Programme on Radioactive Waste Management (EURAD), the Influence of Temperature on Clay-based Material Behaviour (HITEC) work package invited seven teams from across Europe to participate in a benchmark initiative to assess the expertise and capabilities of these teams and their numerical tools to predict THM evolution in different clay materials. The results of this benchmark showed that all teams involved were able to adequately model the THM behaviour of heat-generating repository systems in clay formations, and the tools they used can be considered verified for the solution of coupled THM equations under variable boundary conditions relevant for nuclear waste disposal.

Keywords Boom clay · Callovo–Oxfordian clay · Geological disposal · High-level radioactive waste · Opalinus Clay · Safety assessment · Thermo-hydro-mechanical modelling

1 Introduction

Argillaceous formations are considered across Europe as a potential host for the geological disposal of radioactive waste. This is due to their self-sealing properties, their low permeability, their small molecular diffusion and their retention capacity for radionuclides. Thermo-hydro-mechanical processes (THM processes) play an important role in the evolution of a repository in clay formations. The excavation of the repository mine leads to a damaged zone in the surrounding host geological formation. This excavation-damaged zone is characterized by a higher hydraulic conductivity that enhances hydraulic flow within the repository. Moreover, the heat generated by the waste leads to thermally induced stresses in the rock and potentially further increases the excavation-damaged zone. The heat propagation also gives rise to excess pore pressures in the host clayey formation due to the dilation of water in the porous host medium that may lead to tensile damage even in the far field of the repository system. A deep understanding of the THM behaviour of potential host clayey formations is therefore important for the design and safety assessment of repository systems in these formations.

The assessment of the long-term safety of repository systems requires the use of numerical models and tools capable of reproducing the THM behaviour of the clay host

---

Eric Simo, Christophe de Lesquen, Rocio Paola Leon-Vargas, Minh-ngoc Vu, Simon Raude, Ginger El Tabbal, Arnaud Dizier, Suresh Seetharam, Asta Narkuniene, Frédéric Collin, Hangbiao Song, Antonio Gens, Fei Song, Alexandru-Bogdan Tatomir, Thomas Nagel, Jörg Buchwald have contributed equally to this work.

Extended author information available on the last page of the article rock that has been observed through experimental investigations and predicting the THM evolution of the repository systems over the assessment period of up to one million years. It follows that the reliability of such predictive tools should be verified and validated [14]. Verification is the initial step towards validation, which will subsequently involve the comparison with in situ data from field experiments-endeavours. By verification, one means the mathematical correctness of a given numerical model. To verify such models, one can, for example, compare the output of numerical simulations against their analytic counterparts for a given problem.

Given the increased complexity of numerical models employed in the realm of THM coupled safety assessment of deep geological repositories in clay, there are little analytic solutions against which computer codes can be verified. Ensuring the validity of simulation results and the subsequent reliability of decision-making become therefore increasingly challenging. This predicament is further compounded when multiple numerical codes are employed, adhering to the two-person rule during numerical analyses. Regrettably, no comprehensive guidelines or standards have been published to address the quality of research and commercial codes currently utilized in the safety assessment of repositories worldwide.

Several benchmarking initiatives have been carried out internationally in various research projects to address verification by code comparison on specific topics relevant to the safety assessment of repository, see DECOVALEX [1–3], BENVASIM [13, 16], Reactive Transport Model Benchmarking [10, 12]. In the scope of the project HITEC as part of the European joint programme on radioactive waste (EURAD), seven modelling teams from across Europe were invited to participate in a benchmark initiative to assess the expertise and capabilities of those teams and their numerical tools to predict the THM evolution in different clay host rocks in the near field and the far field of the disposal zone. They present realistic numerical benchmarks of typical safety assessment problems aiming at demonstrating that the different codes commonly employed in Europe yield consistent results. Consequently, based on the findings, these codes can be deemed verified within the framework of "Validation & Verification" (V&V). The results of this benchmarking initiative are the subject of the present paper.

2 Presentation of the work package HITEC of EURAD

HITEC is the acronym for "Influence of Temperature on Clay-based Material Behaviour" that is the seventh work package (WP) of the EURAD Project. The EURAD project is a European joint programme on radioactive waste management that helps to develop a robust and sustained science, technology and knowledge management programme that supports the timely implementation of radioactive waste management (RWM) activities of the EU member states and serves to foster mutual understanding and trust between Joint Programme participants [8]. The work package HITEC of EURAD aims to develop and document an improved thermo-hydro-mechanical (THM) understanding of clay-based materials (host rocks and buffers) exposed at high temperatures ($>100\,^\circ$C) or having experienced high-temperature transients for extended durations. The WP's raison d'être is to evaluate whether or not elevated temperature limits (of $100-150\,^\circ$C) are feasible for a variety of geological disposal concepts for heat-generating radioactive waste. HITEC studies clay host rock formations exposed to temperatures of up to $120\,^\circ$C, documents and establishes the possible extent of elevated temperature damage in the near or far field and also indicates the likely consequences of any such damage. The WP also looks at bentonite buffers and determines the temperature influence on buffer swelling pressure, hydraulic conductivity, erosion or transport properties to see when the buffer safety functions start to be unacceptably impaired [8].

For the disposal of heat-generating radioactive waste, it is important to understand the consequences of the heat produced on the properties of the natural and engineered clay barriers and on their long-term performance. Most safety cases for disposal concepts that involve clay currently consider a temperature limit of $90-100\,^\circ$C. Being able to tolerate higher temperatures, whilst still ensuring an appropriate performance, would have significant advantages (e.g. shorter cooling times at surface intermediate storage facilities, more efficient packaging, fewer disposal containers, fewer transport operations, smaller facility footprints, etc.). This WP interrogates the validity of the currently applied thermal limits and also the importance of the accuracy of the assumed radiological waste properties and consequently marks a first step towards optimization of the architecture of deep geological disposal facilities [8].

Laboratory experiments carried out in the scope of WP HITEC are studying the effects of increased temperature in the near field, such as fracturing and self-sealing in the excavated-damaged zone (subtask 2.1), while other dedicated experiments are looking at the far-field effects, where thermal loading and the generation of overpressures may result in the loss of integrity of the geological barrier (subtask 2.2). Subtask 2.3 is focusing on the modelling of these effects. Two sets of 2D models were created to study the impact of temperature on the behaviour of the three clayey host formations (Boom Clay, Callovo–Oxfordian (COx) claystone and Opalinus Clay (OPA)) in the near field and in the far field. Some of the laboratory experiments were also simulated to improve the understanding of their THM behaviour. Three in situ heating tests (PRACLAY in the Boom Clay, FE in the Opalinus Clay and ALC1605 in the COx) were finally modelled, taking into account the results from the first two steps. The present work describes the results of 2D benchmark studies that have been realized to test the numerical capabilities available across Europe to model the THM behaviour of the three clay host rocks [8].

3 Benchmark description

The benchmarking exercise selected for this work consists of modelling the near-field effects of excavation and heating around the disposal gallery in a repository for radioactive waste in a clay formation. The disposal concept chosen here is inspired by the Swiss and French repository concepts. In the Swiss design, the gallery will be backfilled with bentonite, whereas the French one leaves some room to facilitate a possible retrieval of the waste packages. In addition, the highly exothermic packages are separated by spacing buffers to reduce the thermal load. In order to focus on the host rocks and to be able to compare the models, the boundary condition around the gallery is set at the interface between the gallery and the host rock [8].

Three subcases are proposed [8]:

- Isotropic stress conditions with isotropic thermo-elasticity
- Anisotropic stress conditions with cross-anisotropic (i.e. transversely isotropic) thermo-elasticity
- Anisotropic stress conditions with elastoplastic/damage models (the choice of the model is left to the modelling teams)

The present work will focus on the first two subcases whereas the third case will be the subject of further publications. The goal with the first two subcases is first to compare the numerical codes on a fixed exercise by tightly imposing the boundary conditions and the mechanical constitutive laws and properties.

The first subcase refers to a simple elastic isotropic case, which considers isotropic hydraulic, mechanical and thermal host rock properties as well as an isotropic far-field stress field. The fully coupled thermal-hydro-mechanical (THM) elastic behaviour of Callovo–Oxfordian claystone, Boom Clay and Opalinus Clay is analysed. The isotropic host rock properties are collected in Table 1. The second subcase takes into account the anisotropy of the host rocks' properties and the in situ stress field. The principal directions are oriented parallel and perpendicular to the bedding plane that is assumed, for all three host rocks, coincident with the horizontal and vertical directions, respectively. Along the vertical principal direction, all host rocks exhibit lower intrinsic permeability, elastic modulus and thermal properties. The anisotropic host rock properties are collected in Table 2. Solid and water phase properties are the same as in the isotropic elastic case.

Table 1 Isotropic thermo-hydro-mechanical parameters for the Callovo–Oxfordian claystone, Opalinus and Boom Clay [8]

Parameters	Units	COx	OPA	Boom Clay
Solid phase density ρ_S	kg m^{-3}	2690	2340	2639
Saturated bulk density ρ	kg m^{-3}	2386	2030	2000
Porosity n	–	0.18	0.13	0.39
Intrinsic perm. K	m^2	$2.30 \cdot 10^{-20}$	$3.0 \cdot 10^{-20}$	$2.83 \cdot 10^{-19}$
Young's modulus E	MPa	7000	6000	300
Poisson's ratio v	–	0.3	0.3	0.125
Biot coefficient β	–	0.8	0.6	1
Thermal conductivity λ	$Wm^{-1} K^{-1}$	1.67	1.85	1.47
Linear thermal expansion coefficient α_s	K^{-1}	$1.25 \cdot 10^{-5}$	$1.7 \cdot 10^{-5}$	$1.0 \cdot 10^{-5}$
Solid specific heat capacity c_p	$Jkg^{-1} K^{-1}$	790	995	769

As already mentioned, the model consists of a cross section of a heating gallery and host rock perpendicular to the gallery axis. Due to symmetry, only a quarter of the gallery cross section is modelled. The simulated region measures 100 m in both x and y directions and a plane strain condition ($\epsilon_{z\{x,y,z\}} = 0$) is adopted. A representation of the domain is shown in Fig. 1 together with the specified

Table 2 Anisotropic thermo-hydro-mechanical parameters for the Callovo–Oxfordian claystone, Opalinus and Boom Clay [8]

Parameters	Units	COx	OPA	Boom Clay
$K \parallel$ to bedding	m^2	$3.9 \cdot 10^{-20}$	$5 \cdot 10^{-20}$	$4 \cdot 10^{-19}$
$K \perp$ to bedding	m^2	$1.3 \cdot 10^{-20}$	$1 \cdot 10^{-20}$	$2 \cdot 10^{-19}$
$E \parallel$ to bedding	MPa	8000	8000	400
$E \perp$ to bedding	MPa	5000	4000	200
$v \parallel$ to bedding ($v_{\parallel\parallel}$)	–	0.21	0.35	0.125
$v \perp$ to bedding ($v_{\perp\parallel}$)	–	0.35	0.25	0.25
$G \perp$ to bedding	MPa	2500	2300	80
$\lambda \parallel$ to bedding	$Wm^{-1}K^{-1}$	1.88	2.4	1.65
$\lambda \perp$ to bedding	$Wm^{-1}K^{-1}$	1.25	1.3	1.31

observation points. The corresponding coordinates of these points are summarized in Table 5.

The initial and boundary conditions are divided into three phases to reproduce the evolution of the THM behaviour in the near field of the gallery from the excavation of the gallery up to the heating of the rock (compare Fig. 2).

Excavation phase: The total stress at the gallery wall AE is linearly decreased in 24 h from the initial stress to 5% for COx and OPA and to 50% for Boom Clay, while the total in situ horizontal stress remains constant along CB and the total in situ vertical stress is prescribed on CD. Dirichlet boundary conditions are assigned to the symmetry boundaries AB and DE. The pore water pressure at the gallery wall is linearly reduced in 24 h to 0.1 MPa, while on boundaries BC and CD a constant pore pressure of 4.7 MPa for COx and OPA and 2.25 MPa for Boom Clay is prescribed. Impervious boundaries are assigned on the symmetry boundaries AB and DE.

Waiting phase: The boundary conditions remain unchanged with respect to the end of the excavation phase and are held for six months, allowing water to drain towards the tunnel. No thermal flux is applied at this stage.

Heating phase: The mechanical boundary conditions are similar to the previous phases. Impervious hydraulic boundary conditions are now assigned to the gallery wall. In this phase, a heat flux of 200 Wm^{-1} is applied to the gallery wall over a period of ten years.

The initial and boundary conditions are summarized in Tables 3 and 4. The boundary conditions around the gallery are set at the interface between the gallery and the host rock.

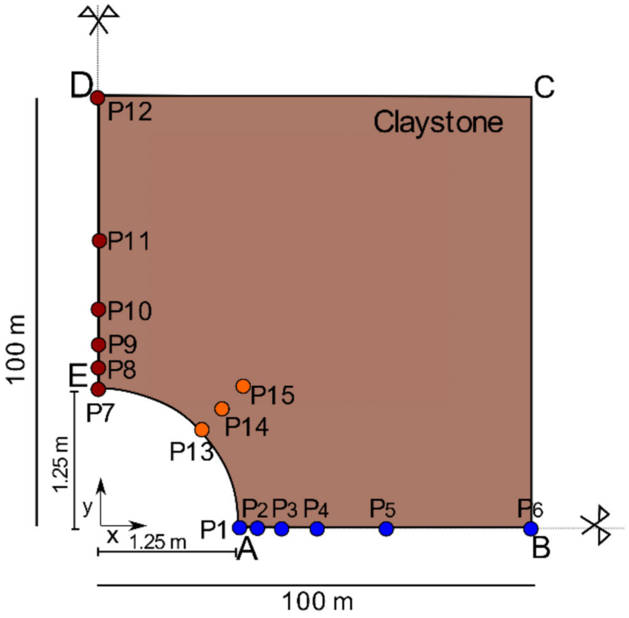

Fig. 1 Observation points in the analysis domain, see Table 5 for coordinates [8]

The water properties to be considered in this benchmarking exercise are a density of 1000 kg m^{-3}, a specific heat capacity of 4180 $\mathrm{Jkg}^{-1}\ \mathrm{K}^{-1}$ and a compressibility at 40 °C of $4.5 \cdot 10^{-4}\ \mathrm{MPa}^{-1}$. The evolution of the volumetric thermal expansion coefficient of water is given as a polynomial fit of temperature under atmospheric pressure following the Eq. [11]:

$$\alpha_w 10^{-4}[^\circ\mathrm{C}^{-1}] = 4 \cdot 10^{-6}[^\circ\mathrm{C}^{-4}]T^3 - 0.001[^\circ\mathrm{C}^{-3}]T^2 + 0.1404[^\circ\mathrm{C}^{-2}]T - 0.3795[^\circ\mathrm{C}^{-1}]$$

with T being the temperature in °C.

The evolution of the water viscosity as a function of the temperature under atmospheric conditions is approximated using Vogel's formula:

$$\mu = \exp\left(A + \frac{B}{C + T}\right)$$

with T being the temperature in K and μ in mPas^{-1}. The fitting parameters have the following values: $A = -3.719[-]$, $B = 578.919\,\mathrm{K}$ and $C = -137.546\,\mathrm{K}$ [9]

Seven modelling teams from across Europe were requested to build a near-field 2D generic model to simulate the three subcases presented above. The teams were organized in such a way that each host rock was studied by several teams and thus allowing a comparison of results and increasing confidence in the modelling work. The teams were ANDRA, BGE, EDF, EIG EURIDICE, LEI, University of Liège and UPC Barcelona. Table 6 gives an overview of the different teams and their corresponding codes. In total six numerical codes have been used by the different teams for the modelling of the different benchmarks.

4 Implementation of thermo-hydro-mechanical (THM) models in various numerical codes

In the implementation of thermo-hydro-mechanical (THM) governing equations for porous media, the various numerical codes involved in this benchmark adopt different methodologies based on their core numerical strategies and intended applications. Below, we discuss the key features of the THM equations implemented in the codes FLAC3D, OpenGeoSys, COMSOL, LAGAMINE, Code_Aster, and Code_Bright. We use capital letters for the divergence (Div) and gradient (Grad) operators to clearly distinguish

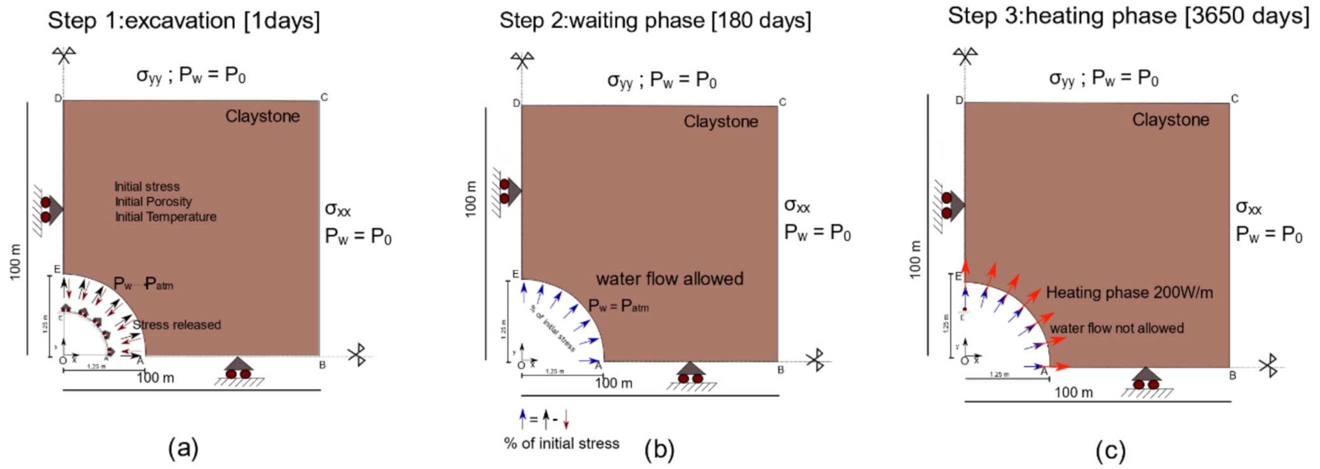

Fig. 2 Boundary conditions at different stages of the analyses [8]

Table 3 Summary of the boundary conditions applied on the gallery wall (compare Fig. 2) [8]

Phases	Mechanical conditions	Hydraulic conditions	Thermal conditions
$T_0 - (T_0 + 24\,\mathrm{h})$: excavation	σ release up to 5 % of the initial in situ stress for COx and OPA, and up to 50 % for Boom Clay	$P_0 \rightarrow P_{\mathrm{atm}}$ (0.1 MPa) in 24 h	No flow at the borehole wall
$(T_0 + 24\,\mathrm{h}) - (T_0 + 6\,\mathrm{months})$: waiting	σ at 5 % of the initial in situ stress	$P_0 = P_{\mathrm{atm}}$	As above
$(T_0 + 6\,\mathrm{months}) - (T_0 + 10\,\mathrm{years})$: heating	As above	No flow	Const. power (200 Wm^{-1})

between the Lagrangian formulation (following a moving material point) and the Eulerian formulation (focused on a fixed spatial point). This convention helps to avoid confusion and emphasizes the specific frame of reference being used in the different codes.

4.1 Energy balance

In CODE_ASTER the energy balance derived by [7] as presented in the previous section is expressed in the Lagrangian framework by:

$$\underbrace{\sum_{p,c} h_c^{mp} m_c^p}_{\text{Energy transfer due to mass}} + \underbrace{\dot{Q}'}_{\text{External heat source}} + \underbrace{\sum_{p,c} \mathrm{Div}\left(h_c^{mp} M_c^p\right)}_{\text{Divergence of enthalpy flux}}$$

$$+ \underbrace{\mathrm{Div}\,\mathbf{q}}_{\text{Divergence of heat flux}} - \underbrace{\sum_{p,c} M_c^p \cdot \mathbf{F}^m}_{\text{Work done by mass forces}} = \underbrace{\Theta}_{\text{Energy dissipation term}}$$

Table 4 Assumed initial conditions in the three host rocks [8]

Parameters	Components	COX	OPA	Boom Clay
Isotropic case				
Total stress MPa	σ_0	12.5	12.5	4.5
Pore pressure MPa	P_0	4.7	4.7	2.25
Temperature °C	T_0	22	22	16.5
Anisotropic case				
Total stress MPa	σ_{xx}	12.4	2.2	3.825
	σ_{yy}	12.7	4.0	4.5
	σ_{zz}	16.4	6.5	3.825
Pore pressure MPa	P_0	4.7	2.1	2.25
Temperature °C	T_0	22	22	16.5

where h_c^{mp} represents the specific enthalpy of component c in phase p; m_c^p denotes the mass of component c in phase p; $\dot{Q}'$ is the rate of heat addition from an external source; $\mathrm{Div}\left(h_c^{mp} M_c^p\right)$ indicates the divergence of the enthalpy flux of component c in phase p; Div $\mathbf{q}$ is the divergence of the

Table 5 Coordinates of observation points in meter

Points	Coordinates	Points	Coordinates
P1	(1.25, 0.0)	P8	(0.0, 1.9)
P2	(1.9, 0.0)	P9	(0.0, 2.5)
P3	(2.5, 0.0)	P10	(0.0, 6.25)
P4	(6.25, 0.0)	P11	(0.0, 50.0)
P5	(50.0, 0.0)	P12	(0.0, 100.0)
P6	(100.0, 0.0)	P13	(0.88, 0.88)
P7	(0.0, 1.25)	P14	(1.33, 1.33)
		P15	(1.77, 1.77)

Table 6 Involved modelling teams and their respective codes

Organization	Country	Numerical code	Boom Clay	COx	OPA
ANDRA	France	COMSOL, Code_Aster		✓	
BGE	Germany	OpenGeoSys, FLAC3D	✓	✓	✓
EDF	France	Code_Aster		✓	✓
EIG EURIDICE	Belgium	COMSOL	✓		
LEI	Lithuania	COMSOL		✓	
ULiege	Belgium	Lagamine	✓	✓	
UPC	Spain	CODE_BRIGHT		✓	✓

heat flux vector $\mathbf{q}$; M_c^p represents the hydraulic flux of component c in phase p, corresponding to w in the Eulerian configuration; $\mathbf{F}^m$ denotes the force per unit mass acting on the components due to external fields; and Θ represents the energy dissipation term, accounting for heat generation and internal dissipation.

In LAGAMINE, the energy balance equation is formulated in a weak form for an arbitrary virtual temperature field T^* within the current deformed configuration Ω^t, whose boundary is denoted by Γ_σ^t.:

$$\int_{\Omega^t}\left(\underbrace{\dot{S}_T^t}_{\text{Enthalpy evolution}} T^* - \underbrace{f_{T,i}^t}_{\text{Heat flow}} \frac{\partial T^*}{\partial x_i^t}\right) d\Omega^t = \int_{\Omega^t} \underbrace{Q_T^t}_{\text{Heat sink term}} T^* d\Omega^t - \int_{\Gamma_{q_T}^t} \underbrace{\vec{q}_T^t}_{\text{heat flux}} T^* d\Gamma^t$$

In Code_Bright, the balance of internal energy for the medium is defined by:

$$\frac{\partial}{\partial t}\left[\underbrace{E_S\rho_S(1-\phi)}_{\substack{\text{Energy of the}\\ \text{solid phase}}} + \underbrace{E_l\rho_l S_l\phi}_{\substack{\text{Energy of the}\\ \text{liquid phase}}} + \underbrace{E_g\rho_g S_g\phi}_{\substack{\text{Energy of the}\\ \text{gas phase}}}\right] + \operatorname{div}\underbrace{\left(i_i^c + j_j^{Es} + j_j^{El} + j_j^{Eg}\right)}_{\substack{\text{Energy fluxes :}\\ \text{conduction and advection}}} = \underbrace{f^Q}_{\substack{\text{Internal or external}\\ \text{energy supply}}}$$

where i_i^c denotes the conductive energy flux within the porous medium; f^Q represents sources of energy, both internal and external; j_i^E corresponds to the advective energy flux resulting from mass movement; and E signifies the specific internal energy.

In COMSOL, we have:

$$\frac{\partial}{\partial t}\left[\underbrace{\rho c_p T}_{\substack{\text{Energy storage term}\\ \text{(heat capacity)}}}\right] + \underbrace{\operatorname{div}(-\lambda \operatorname{grad} T)}_{\substack{\text{Divergence of heat flux}\\ \text{(conduction)}}} + \underbrace{\operatorname{div}(\rho c_p \mathbf{u} T)}_{\substack{\text{Divergence of convective}\\ \text{heat transfer}}} = \underbrace{Q}_{\substack{\text{Heat source}\\ \text{or sink}}}$$

in FLAC3D the thermal energy balance is expressed as:

Table 7 Correspondence of energy balance terms across software

Concept	LAGAMINE	Code_Aster	Code_Bright	COMSOL	FLAC3D	OpenGeoSys
Energy storage	$\dot{S}_T^t T$	$\operatorname{Div}\left(h_c^{mp} M_c^p\right) - \Theta$	$E_S\rho_S(1-\phi) + E_l\rho_1 S_1\phi + E_g\rho_g S_g\phi$	$\rho c_p T$	ξ^T	$\rho c_p T$
Heat flux (conductive)	$f_{T,i}^t$	$\mathbf{q}$	i_i^c	$-\lambda$ grad T	q_i^T	$-\lambda$ grad T
Divergence of heat flux	$\vec{q}_T^t$	$\operatorname{Div}\mathbf{q}$	$\operatorname{div}(i_i^c + j_j^{Es} + j_j^{El} + j_j^{Eg})$	$\operatorname{div}(-\lambda \operatorname{grad} T)$	$\operatorname{Div}(q_i^T)$	$\operatorname{div}(-\lambda \operatorname{grad} T)$
Heat flux (advective)	–	$\sum_{p,c} h_c^{mp} m_c^p$	$j_j^{Es} + j_j^{El} + j_j^{Eg}$	$\operatorname{Div}(\rho c_p \mathbf{u} T)$	–	$\operatorname{div}(\rho c_p \mathbf{u} T)$
Heat source or sink	Q_T^t	$\dot{Q}'$	f^Q	Q	q_v^T	Q

$$\underbrace{-\text{Div}\ q_i^T}_{\substack{\text{Heat flux}\\ \text{divergence}}} + \underbrace{q_\text{v}^T}_{\substack{\text{Volumetric heat}\\ \text{source intensity}}} = \underbrace{\frac{\partial \xi^T}{\partial t}}_{\substack{\text{Rate of heat storage}\\ \text{per unit volume}}}$$

Two process models in OpenGeoSys were employed in this benchmarking: a non-isothermal Richards flow model coupled with mechanics, and a thermo-hydraulic (TH) model using thermo-mechanical storage coefficients [5]. The first model follows a monolithic approach, deriving hydraulic-mechanical couplings from three-dimensional effective stress and omitting vapour diffusion based on benchmark assumptions. The second TH model incorporates mechanical effects within the mass balance of the TH process via thermo-mechanical storage coefficients, assuming uniaxial strain ($\epsilon_{xx} = \epsilon_{yy} = 0$) and constant vertical stress (σ_{zz}), while also considering thermal stresses from constrained transverse thermal expansion. The energy balance for the non-isothermal Richards flow model is given below:

$$\underbrace{\frac{\partial}{\partial t}\left[\rho c_p T\right]}_{\substack{\text{Energy storage}\\ \text{(heat capacity)}}} + \underbrace{\text{div}(-\lambda\,\text{grad}T)}_{\substack{\text{Divergence of}\\ \text{heat flux (conduction)}}}$$

$$+ \underbrace{\text{div}\left(\rho c_p \mathbf{u} T\right)}_{\substack{\text{Convective}\\ \text{heat transfer}}} = \underbrace{Q}_{\substack{\text{Heat source}\\ \text{or sink}}}$$

Table 7 provides a concise comparison of energy balance components across six THM simulation software: LAGAMINE, Code_Aster, Code_Bright, COMSOL, FLAC3D, and OpenGeoSys, each employing unique formulations. Energy storage is represented differently, with LAGAMINE and Code_Bright considering phase-specific energies, while COMSOL, OpenGeoSys, and FLAC3D use simpler forms such as $\rho c_p T$. Code_Aster employs a divergence term related to enthalpy flux. Heat flow (conduction) is consistently expressed via Fourier's law across software, commonly as $-\lambda$ grad T, with specific forms like $f_{T,i}^t$ in LAGAMINE and i_i^c in Code_Bright. Heat flux divergence describes the distribution of conductive heat, often using divergence operators; Code_Bright uniquely integrates conduction and advection to account for multiphase effects. Convective heat transfer, noted in Code_Aster, Code_Bright, COMSOL, and OpenGeoSys, includes heat transported by fluid flow, while FLAC3D omits this term, focusing on solid mechanics. Each software includes a heat source or sink term, with labels as Q_T^t (LAGAMINE), $\dot{Q}'$ (Code_Aster), f^Q (Code_Bright), Q (COMSOL, OpenGeoSys), and q_v^T (FLAC3D), allowing for a range of energy interactions. This overview emphasizes each software's adaptability, from simplified single-phase models to multi-phase approaches for comprehensive THM simulations.

4.2 Fluid mass balance

In LAGAMINE, The fluid mass balance equation is expressed in a weak form for any admissible virtual pore pressure field p_w^*:

$$\int_{\Omega^t}\left(\underbrace{\dot{M}_w^t p_w^*}_{\substack{\text{Time derivative}\\ \text{of fluid mass}}} - \underbrace{f_{w,i}^t \frac{\partial p_w^*}{\partial x_i^t}}_{\substack{\text{Mass flow}\\ \text{gradient}}}\right) d\Omega^t$$

$$= \int_{\Omega^t} \underbrace{Q_w^t p_w^*}_{\text{Fluid sink term}} d\Omega^t - \int_{\Gamma_{q_w}^t} \underbrace{\bar{q}_w^t p_w^*}_{\substack{\text{Boundary}\\ \text{mass flux}}} d\Gamma^t$$

Here, $f_{w,i}^t$ represents the mass flow rate, Q_w^t denotes a term accounting for fluid sinks, and $\Gamma_{q_w}^t$ is the boundary segment where the incoming fluid mass per unit area, given by $\bar{q}_w^t$, is specified. Additionally, $\dot{M}_w^t$ denotes the time rate of change of fluid mass.

The fluid mass balance in FLAC3D is defined by:

$$\underbrace{-\text{Div}\ q_i}_{\substack{\text{Divergence of}\\ \text{fluid flux}}} + \underbrace{q_\text{v}}_{\substack{\text{Volumetric fluid}\\ \text{source intensity}}} = \underbrace{\frac{\partial \zeta}{\partial t}}_{\substack{\text{Time derivative}\\ \text{of fluid content}}}$$

In COMSOL, the water mass (m_w) balance equation includes additional water source terms to take into account the different coupling processes (HM, TH and TM) and is expressed as follows:

$$\underbrace{\frac{\partial m_\text{w}}{\partial t}}_{\text{Time derivative of water mass}} + \underbrace{\text{div}(\rho_w \mathbf{q}_\text{w})}_{\substack{\text{Divergence of mass flux}\\ \text{due to water flow}}}$$

$$= \underbrace{Q_\text{H}}_{\text{Water source}}$$

In Code_Bright, The total mass balance of water in the liquid phase is given by:

Table 8 Correspondence of fluid mass balance terms across THM codes

Concept	LAGAMINE	Code_Aster	Code_Bright	COMSOL	FLAC3D	OpenGeoSys
Time derivative of mass	$\dot{M}_w^t$	$\partial m_w/\partial t$	$\frac{\partial}{\partial t}\left[\omega_l^w \rho_l S_l \phi + \omega_g^w \rho_g S_g \phi\right]$	$\partial m_w/\partial t$	$\partial \zeta/\partial t$	$\partial m_w/\partial t$
Mass flow / flux	$f_{w,i}^t/\partial x_i^t$	$\partial M_{w,i}/\partial x_i$	$j_{i,i}^{l,w} + j_{i,i}^{g,w}$	div $(\rho_w \mathbf{u})$	$-$Div q_i	div $\mathbf{j}_w$
Volumetric source / sink term	Q_w^t	q_v	f^w	Q_H	q_v	q_v
Boundary mass flux	$\bar{q}_w^t$	–	–	–	–	–

$$\underbrace{\frac{\partial}{\partial t}\left[\omega_\mathrm{l}^w \rho_\mathrm{l} S_\mathrm{l} \phi + \omega_\mathrm{g}^w \rho_\mathrm{g} S_\mathrm{g} \phi\right]}_{\substack{\text{Rate of change of water mass}\\ \text{in liquid and gas phases}}} + \underbrace{\left(j_{i,i}^{l,w} + j_{i,i}^{g,w}\right)}_{\substack{\text{Divergence of water mass}\\ \text{flux in liquid and gas phases}}} = \underbrace{f^w}_{\text{External water supply}}$$

Here, ω_l^w and ω_g^w represent the mass fraction of the component (water) relative to the total mass of the liquid and gas phases, respectively. S_l and S_g are the saturation degrees of the liquid and gas phases, indicating the fraction of pore volume each phase occupies. ρ_l and ρ_g denote the densities of the liquid and gas phases, respectively. $j_i^{l,w}$ represents the mass flux of water within the liquid phase, while $j_i^{g,w}$ represents the mass flux of water within the gas phase. Lastly, f^w indicates an external water source.

The liquid water mass balance equation for hydraulics in Code_Aster is defined by:

$$\underbrace{\frac{\partial m_\mathrm{w}}{\partial t}}_{\substack{\text{Rate of change of}\\ \text{liquid water mass content}}} + \underbrace{\frac{\partial M_{w,i}}{\partial x_i}}_{\substack{\text{Divergence of}\\ \text{liquid water mass flow}}} = \underbrace{q_\mathrm{v}}_{\substack{\text{Volumetric}\\ \text{source term}}}$$

In OpenGeoSys, the fluid mass balance equation is given by:

$$\underbrace{\frac{\partial m_\mathrm{w}}{\partial t}}_{\substack{\text{Rate of change of}\\ \text{water mass content}}} + \underbrace{\text{div } \mathbf{j}_w}_{\substack{\text{Divergence of}\\ \text{water mass flux}}} = \underbrace{q_\mathrm{v}}_{\substack{\text{Volumetric source}\\ \text{or sink term}}}$$

where:m_w: represents the mass of water per unit volume in the porous medium. $\mathbf{j}_\mathrm{w}$: water mass flux vector, defined by Darcy's law. q_v: volumetric source or sink term, representing water sources or sinks per unit volume.

Table 8 summarizes the correspondence of fluid mass balance terms across different THM codes. In LAGAMINE, the weak form of the fluid mass balance includes explicit terms for the time derivative of fluid mass, mass flow gradient, fluid sink term, and boundary mass flux. In Code_Aster and OpenGeoSys, the formulations emphasize the rate of change of water mass content and divergence of water mass flow, aligning with terms in FLAC3D and COMSOL where fluid storage and transport mechanisms are central. Code_Bright introduces specific terms for the liquid and gas phase fluxes and the external water supply, necessary for multiphase behaviour. These distinctions reflect differences in handling boundary conditions and explicit or implicit source and sink terms across the codes.

4.3 Mechanical balance equation for momentum conservation

The mechanical balance equation, characterizing the conservation of momentum in porous media, considers both the effective stresses within the solid matrix and the body forces acting upon it. This formulation is generally valid across multiple THM modelling codes and is expressed as follows:

$$\sigma_{ij,j} + b_i = 0$$

where σ_{ij} is the component of stress, b_i represents body force.

4.4 Challenges in comparing implementations

Comparing the implementations of THM processes in various numerical codes is challenging due to differences in frameworks (Eulerian vs. Lagrangian), numerical schemes, and handling of multi-physics couplings. Each code has unique methodologies in formulating balance equations, applying weak or strong forms, and managing coupling effects, especially in multiphase flow, thermal conduction, and mechanical deformation. This variability stems from the distinctive use cases each software targets, whether in geotechnical applications, environmental engineering, or multi-phase fluid transport in porous media. Therefore, benchmarking initiatives are essential for verifying and comparing the performance and accuracy of the THM models across different codes.

5 Constitutive equations for the skeleton

In elasticity theory, the Hooke's stress-strain relation is formulated as follows: $\varepsilon_{ij} = C_{ijkl}\,\sigma_{kl}$

where ε and σ are respectively the strain and stress tensor. C_{ijkl} are the coordinates of the fourth-order compliance tensor. **(C)** is the corresponding compliance matrix in Kelvin notation which we will specify below for the materials used in this benchmark..

In the following, we are presenting the compliance matrices of the materials used in this benchmark.

The Isotropic Elastic Compliance Matrix

For linear isotropic elastic materials, the compliance matrix **C**C depends on two independent material properties, such as the Young's modulus E and the Poisson's ratio v. In the most general isotropic form, the compliance matrix is expressed as:

$$\mathbf{C} = \begin{bmatrix} \frac{1}{E} & -\frac{v}{E} & -\frac{v}{E} & 0 & 0 & 0 \\ -\frac{v}{E} & \frac{1}{E} & -\frac{v}{E} & 0 & 0 & 0 \\ -\frac{v}{E} & -\frac{v}{E} & \frac{1}{E} & 0 & 0 & 0 \\ 0 & 0 & 0 & \frac{1}{2G} & 0 & 0 \\ 0 & 0 & 0 & 0 & \frac{1}{2G} & 0 \\ 0 & 0 & 0 & 0 & 0 & \frac{1}{2G} \end{bmatrix}$$

In this expression, the shear modulus G is given by:

$$G = \frac{E}{2(1+v)}$$

Transverse Isotropic Elastic Compliance Matrix

For cross-anisotropic or transverse isotropic elasticity, five independent material parameters are required to describe the elastic behavior:

$E_{||}, E_{\perp}, v_{||\,||}, v_{||\,\perp}, and\, G_{||\,\perp}$ Here, the subscripts

$||\, and \perp$

refer to directions parallel and perpendicular to the isotropic planes, respectively. In this case, the elastic compliance matrix is defined as [17]:

$$\mathbf{C} = \begin{bmatrix} \frac{1}{E_{||}} & -\frac{v_{\perp||}}{E_{\perp}} & -\frac{v_{||||}}{E_{||}} & 0 & 0 & 0 \\ -\frac{v_{||\perp}}{E_{||}} & \frac{1}{E_{\perp}} & -\frac{v_{||\perp}}{E_{||}} & 0 & 0 & 0 \\ -\frac{v_{||||}}{E_{||}} & -\frac{v_{\perp||}}{E_{\perp}} & \frac{1}{E_{||}} & 0 & 0 & 0 \\ 0 & 0 & 0 & \frac{1}{2G_{||\perp}} & 0 & 0 \\ 0 & 0 & 0 & 0 & \frac{1}{2G_{||||}} & 0 \\ 0 & 0 & 0 & 0 & 0 & \frac{1}{2G_{\perp||}} \end{bmatrix}$$

The symmetry of the compliance tensor imposes the following relationship between the Poisson's ratios and Young's moduli:

$\frac{v_{||\perp}}{E_{||}} = \frac{v_{\perp||}}{E_{\perp}}$ The shear modulus in the isotropic planes ($G_{||\,||}$) can be expressed as:

The symmetry of the stress and strain tensors implies that the other shear moduli are equal:

$G_{||\perp} = G_{||||}$

6 Analytical benchmark

The first step towards model verification is to compare the accuracy of the THM models against well-defined analytical solutions. This section presents a benchmark analysis for the analytical solution of the coupled thermo-hydro-mechanical (THM) consolidation problem, originally derived by [4] and later corrected for the effective stress term by [6]. The aim of this benchmark is to validate the theoretical formulation of the involved THM models through coordinated efforts by several teams. The benchmark analysis will focus on three primary variables: temperature, pore pressure, and displacement of the solid skeleton.

Problem overview

The problem describes a heat source embedded in a fully fluid-saturated porous medium. Due to spherical

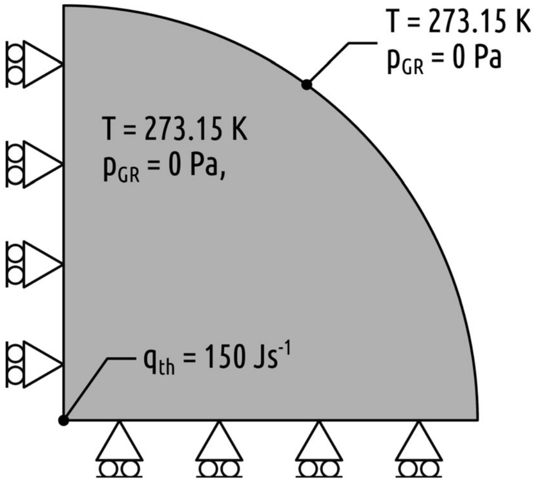

Fig. 3 Numerical model setup of the point heat source problem [15]

symmetry, the system is modelled using a 10 m × 10-m disc with a point heat source (Q=150 W) placed at one corner and a curved boundary at the opposite edge. By applying rotational axial symmetry along one of the linear boundaries, the model region is transformed into a half-space representation of the spherical symmetrical problem, corresponding to the analytical solution. The initial temperature and excess pore pressure are set to 273.15 K and 0 Pa, respectively. The axis-normal displacements along the symmetry (inner) boundaries are constrained to zero, while the temperature and excess pore pressure are held at their initial values along the outer (curved) boundary. Heat from the point source propagates through the medium, causing both the fluid and solid phases to expand at different rates. This differential expansion results in a pore pressure gradient, which drives a thermally induced consolidation process as the fluid moves away from the heat source until equilibrium is reached [15]. The numerical model for this problem is depicted in Fig. 3

Table 9 Material parameters used in the analytical benchmark [15]

Parameter	Value	Unit
Permeability (k_s)	2.0×10^{-20}	m^2
Porosity (Φ)	0.16	–
Liquid phase density (ρ_w)	999.1	kg m^{-3}
Solid phase density (ρ_s)	2290.0	kg m^{-3}
Liquid phase dynamic viscosity (μ)	1.0×10^{-3}	Pa s
Young's modulus (E)	5.0	GPa
Poisson ratio (ν)	0.3	–
Liquid phase thermal conductivity (λ_w)	0.6	W m^{-1} K^{-1}
Solid phase thermal conductivity (λ_s)	1.838	W m^{-1} K^{-1}
Liquid-phase specific heat capacity (c_w)	4280	J kg^{-1} K^{-1}
Solid-phase specific heat capacity (c_s)	917.654	J kg^{-1} K^{-1}
Liquid thermal (volumetric) expansion (α_w)	4.0×10^{-4}	K^{-1}
Solid thermal (linear) expansion (α_s)	1.5×10^{-5}	K^{-1}

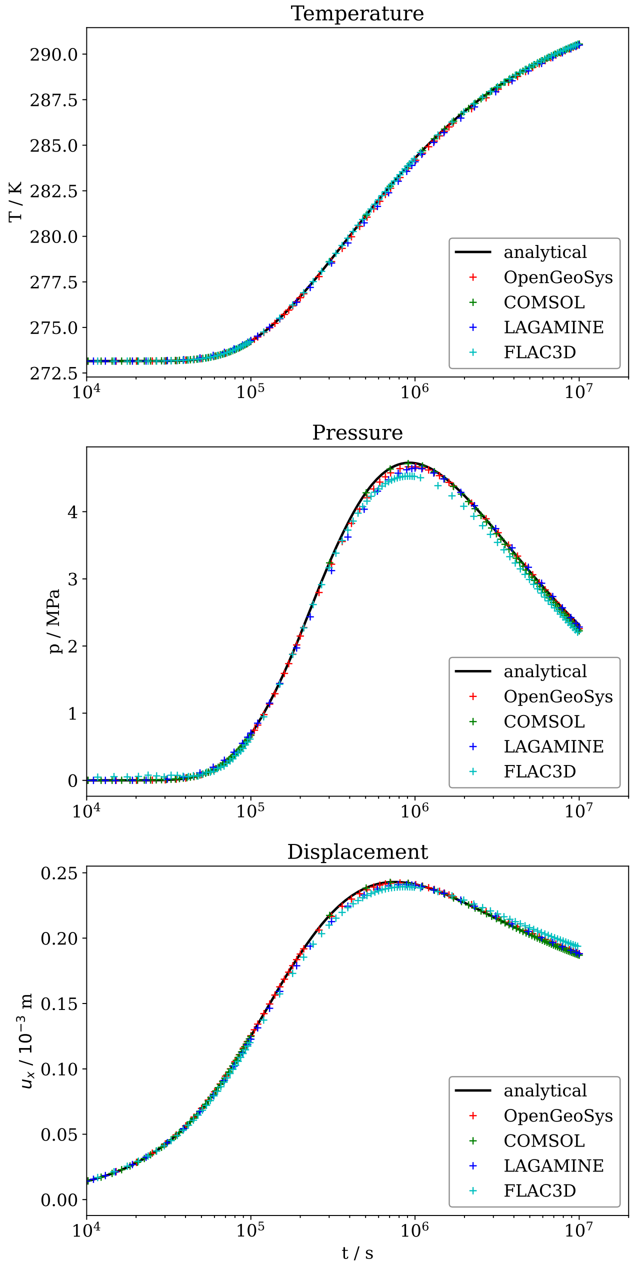

Fig. 4 Obtained numerical results against the reference solutions for the analytical benchmark problem for temperature, pore pressure, radial displacement

Analytical expressions

The following equations describe the analytical solution for the three primary variables:

$$\text{Temperature: } \Delta T = \frac{Q}{4\pi K r} f^{\kappa}$$

$$\text{Pore pressure: } p = \frac{XQ}{(1-\frac{c}{\kappa})4\pi K r}(f^{\kappa} - f^{c})$$

$$\text{Displacement of the Solid Skeleton: } u_i = \frac{Q a_u x_i}{4\pi K r} g^{*}$$

In the above equations, the following derived parameters are used: [15]

$$\kappa = \frac{K}{m}, \quad c = \frac{k_s}{\eta}(\lambda + 2G), \quad r = \sqrt{x_1^2 + x_2^2 + x_3^2}$$

$$X = a_u(\lambda + 2G) - b', \quad Y = \frac{1}{\lambda + 2G}\left(\frac{X}{(1-\frac{c}{\kappa})a_u} + \frac{b'}{a_u}\right)$$

$$Z = \frac{1}{\lambda + 2G}\left(\frac{X}{(1-\frac{c}{\kappa})a_u}\right), \quad f^{A} = \operatorname{erfc}\left(\frac{r}{2\sqrt{At}}\right), \quad A = \kappa, c$$

$$g^{A} = \frac{At}{r^2} + \left(\frac{1}{2} - \frac{At}{r^2}\right)f^{A} - \sqrt{\frac{At}{\pi r^2}}\exp\left(-\frac{r^2}{4At}\right)$$

$$g^{*} = Yg^{\kappa} - Zg^{c}, \quad g_i^{*} = Yg_i^{\kappa} - Zg_i^{c}$$

$$g_i^{A} = \frac{2x_i At}{r^4}\left(f^{A} - 1 + \frac{r}{\sqrt{\pi At}}\exp\left(-\frac{r^2}{4At}\right)\right), \quad i = 1, 2, 3$$

They are obtained from the governing equations by considering the following assumptions [15]:

- Thermal advection effects are not included
- Gravitational effects are disregarded
- Both fluid and solid phases are assumed to be intrinsically incompressible
- There is no external fluid source or sink
- The porous medium is considered isotropic and homogeneous

We considered the following set of values as input parameters, see Table 9:

Benchmark results

The analytical problem was solved numerically using several codes involved in this benchmark initiative. The results were evaluated at an observation point located at a distance of $0.5\sqrt{2}$ from the centre of the sphere, with coordinates (0.5, 0.5, 0). These results are compared with the analytical solution in Fig. 4. The comparison shows an excellent agreement between the numerical and analytical results for the FEM codes OpenGeoSys, COMSOL, and LAGAMINE. However, results from FLAC3D deviates from the rest. FLAC3D required also a much finer mesh to obtain satisfactory results and took significantly more time to compute compared to other codes. It has been observed that the undrained thermal coefficient is highly sensitive in THM simulations using FLAC3D, which likely explains the discrepancies observed. Despite this, the results are sufficiently close to validate the accuracy of the implemented THM models.

7 Numerical benchmark

In the following, we present the results of the THM benchmark simulations for the isotropic and anisotropic cases. These simulations were conducted for each of the three clay host rocks being considered in Europe for the disposal of radioactive waste, resulting in six sets of results.

Mesh configurations

The simulations were performed using a variety of mesh configurations, as shown in Table 10. Teams were given the flexibility to develop meshes based on their own preferences, leading to a diversity of mesh types in this benchmark. Several teams opted for triangular meshes, including ANDRA, BGE, and LEI. In contrast, ULG and UPC employed quadrangular meshes. EDF used a hybrid mesh, combining quadrangular elements in the near field (around the gallery) and triangular elements in the far field.

On average, the meshes consisted of a few thousand elements, with a mean of approximately 3750 elements, excluding the EDF mesh. The EDF mesh was notably the largest, containing 28,666 elements. Except for BGE using OGS, ULG and UPC, which utilized quadratic elements, all other meshes consisted of linear elements.

Table 10 Details of the meshes used for the numerical benchmark

Organization	Code	Mesh type	Mesh size	Mesh order
ANDRA	Code_Aster	Triangular	6594	Linear
ANDRA	COMSOL	Triangular	1828	Linear
BGE	OGS	Triangular	3369	Quadratic
BGE	FLAC3D	Quadrangular	4040	Linear
EDF	Code_Aster	Quadrangular in NF, Triangular in FF	28666	Linear
LEI	COMSOL	Triangular	3461	Linear
ULG	LAGAMINE	Quadrangular	2120	Quadratic
UPC	Code_Bright	Quadrangular	4792	Quadratic

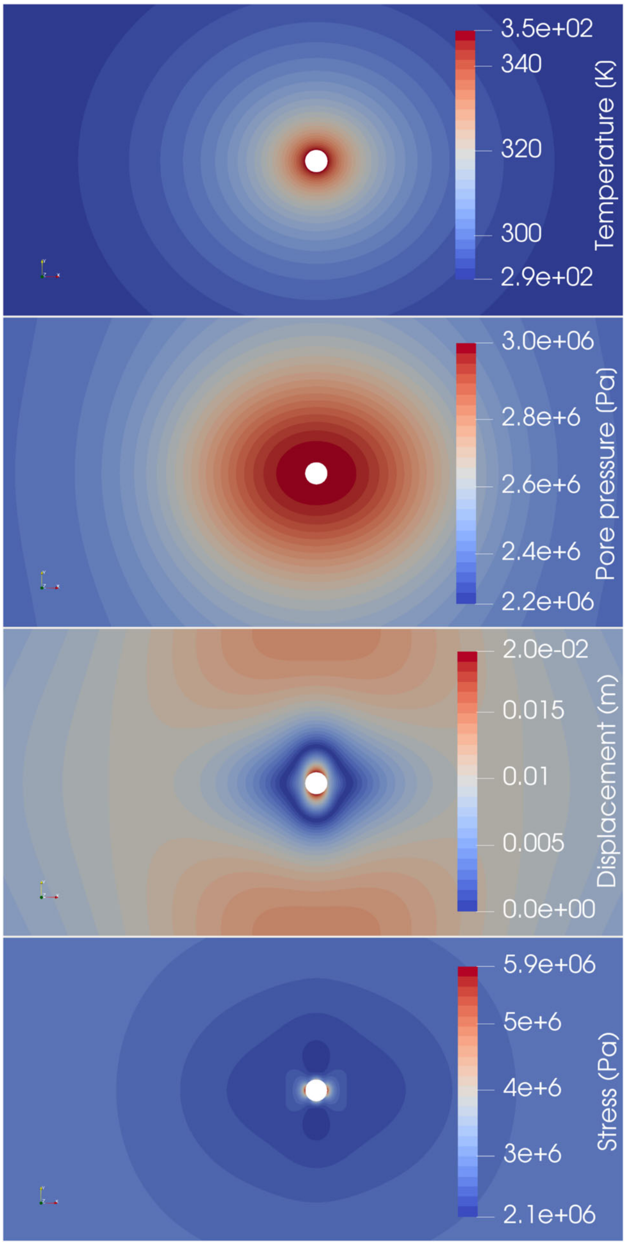

Fig. 5 Evolution of temperature, pore pressure, radial displacement and stress magnitude (in absolute values) after 10 years of heating for the benchmark case in Boom Clay with anisotropic material parameters

Despite the heterogeneity in the mesh structures, all simulations—focused on the elastic cases—were completed in under 5 min across all teams in exception of FLAC3D. Benchmark simulations with FLAC3D required a 3D model leading to higher computational time of up to several days. A more detailed comparison of computational times was deemed unnecessary, as the computing environments varied significantly, ranging from standard office laptops to high-performance computing systems.

Qualitative THM behaviour of the benchmark problem

Generally speaking, similar THM behaviour can be expected for all clay host rocks. Initially, there is a significant increase in radial displacement (convergence) due to excavation. During the waiting phase, the convergence of the rock mass continues to increase. In the heating phase, radial convergence decreases due to the thermal expansion of the rock mass, with the rock farthest from the gallery wall even experiencing displacement away from the gallery. Pore pressure at the gallery wall decreases during the excavation phase, remains constant during the waiting phase, and experiences a significant increase in the heating phase, which is related to the differing rates of thermal expansion between water and rock matrix.

The THM evolution in anisotropic conditions is clearly illustrated for the benchmark case in Boom clay with anisotropic material parameters in Fig. 5, which shows the evolution of temperature, pore pressure, displacement magnitude, and stress magnitude after 10 years of heating. As expected, the temperature and pore pressure disturbances extend farther in the horizontal direction due to the higher thermal conductivity and permeability parallel to the bedding. The evolution of the displacement reveals that the rock mass near the gallery exhibits converging behaviour, while a region with no displacement marks the transition to a region where expansion displacement away from the heat source occurs. The evolution of the stress magnitude shows that the stress redistribution is concentrated around the gallery. These qualitative results are similar for the other host rocks (COx and OPA) and also apply to the isotropic case with the exception that the isolines in the contour plots are circular rather than elliptical.

Benchmark metrics

For the sake of brevity, we will only present quantitative results for four observation points located in the horizontal direction. Six variables are analysed quantitatively: the three primary variables of the THM simulation (displacement, pore pressure, and temperature) and three variables that assess the stress state of the system (the deviatoric stress invariant, the effective vertical stress, and the effective horizontal stress). The modelling teams were requested to provide the effective stress following the Biot effective stress concept. The deviatoric stress was evaluated using the equation:

$$\sqrt{\left(\sigma_{xx}-\sigma_{yy}\right)^{2}+4\sigma_{xy}^{2}}$$

The horizontal and vertical displacement were aggregated into the radial displacement using the equation $u_r = \sqrt{u_x^2 + u_y^2}$. A sign convention was also used for the evaluation of displacement, with increasing values

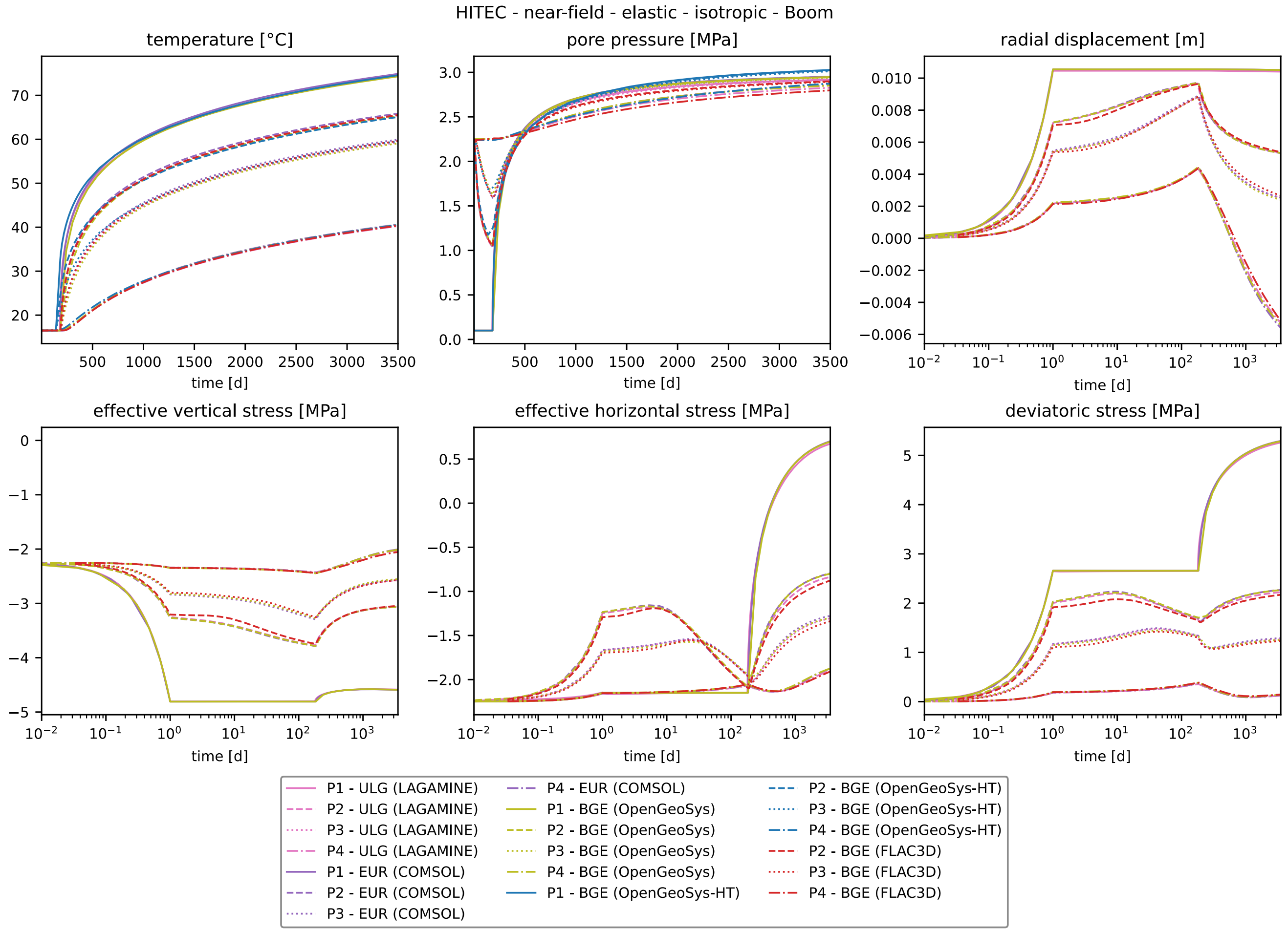

Fig. 6 Benchmark results for the elastic isotropic case in Boom clay [8]

indicating the movement of the rock mass towards the gallery and vice versa. Positive displacement values indicates closer proximity to the gallery after THM loading and vice versa.

7.1 Boom Clay: elastic isotropic case

Figure 6 shows the results for the THM response for the poorly indurated Boom Clay with isotropic material parameters. The teams were composed of ULG, EUR and BGE with three process models. A temperature increase is observed at all observation points during the heating phase starting at 6 months. As expected, the temperature decreases with the distance to the gallery. A maximum temperature of 76 °C was obtained after 10 years of heating at the gallery wall. 40 °C can be measured at P4 located at 5 m from the gallery. The comparison of temperature evolution curves obtained by all teams shows a good agreement. A negligible deviation in the temperature results of BGE computed with FLAC3D is noticeable.

The pore pressure evolution at the observation points shows a decrease in pore pressure at P2 and P3 during the waiting phase in the first six months. In this phase, the model is drained at the gallery wall. This pore pressure decrease vanishes with distance to the gallery wall and is already negligible at P4. At P1 the pore pressure is equal to 0.1 MPa as prescribed for this benchmark, see Table 3. During the heating phase, an increase in pore pressure is observed at all points. This pore overpressure is the result of the thermal pressurization that occurs due to the difference in the thermal expansion of water and solid. At the end of the simulation, a maximum pore pressure of about 3 MPa can be observed at the gallery wall where the temperature is highest. Interestingly, almost the same value is obtained at the observation points P2 and P3. The maximum overpressure at P4 is slightly below and is equal to about 2.8 MPa at the end of the simulation. Overall, all pore pressure evolution curves are consistent for all process models. Small deviations in the BGE results computed with FLAC3D and the hydrothermal model in OpenGeoSys are observed at the end of the heating phase.

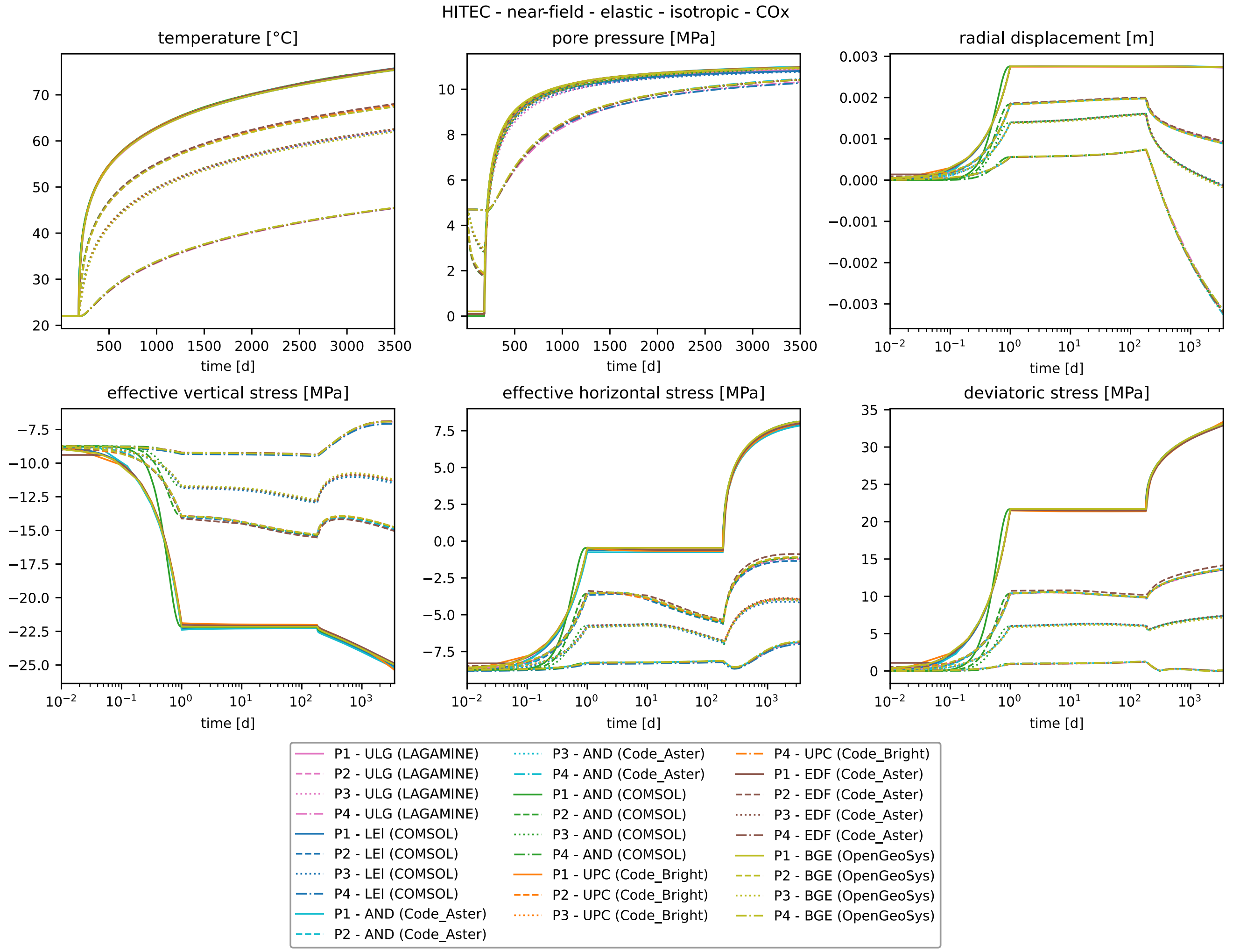

Fig. 7 Benchmark results for the elastic isotropic case in COx claystone [8]

The mechanical behaviour in the model is characterized by displacement and stress evolution. During excavation, displacement at all points increases due to gallery convergence. This increase continues during the waiting phase as drainage progresses. In the heating phase, there is a change in the direction of displacement, with movement away from the gallery wall due to the thermal expansion of the rock mass. At the end of the simulation, the observation point P4 has moved 5 mm deeper into the rock mass, away from the gallery wall. The displacement curves computed by all teams are identical at each point, and this consistency is reflected in the results of stress evolution. The evolution of the vertical and horizontal effective stress, as well as the deviatoric stress, are comparable among all teams involved in this benchmark. However, the results computed with FLAC3D show some oscillations in the waiting phase and deviate slightly from the general trend of other teams. The pore overpressure due to the temperature increase in the heating phase leads to stress relief in the model eventually leading to tensile stresses at P1 in the horizontal direction. These tensile stresses result from sealing the gallery wall during the heating phase as part of the requirements for this benchmark. In repository conditions, the total stress would remain compressive when the gallery is backfilled. However, the tensile stresses appear to be limited to the region near the gallery wall because the horizontal stress state at P2 remains compressive at the end of the simulation.

7.2 Callovo-Oxfordian claystone: elastic isotropic case

The results for the THM benchmark in COx claystone assuming an elastic isotropic mechanical response are presented in Fig. 7 in terms of displacements, pore pressure, temperature and stress evolution. six teams took part in this benchmark with ANDRA participating with two codes. The general trend for the evolution of all variables is similar to the Boom Clay case previously reported. A good agreement in the results obtained by all teams has been

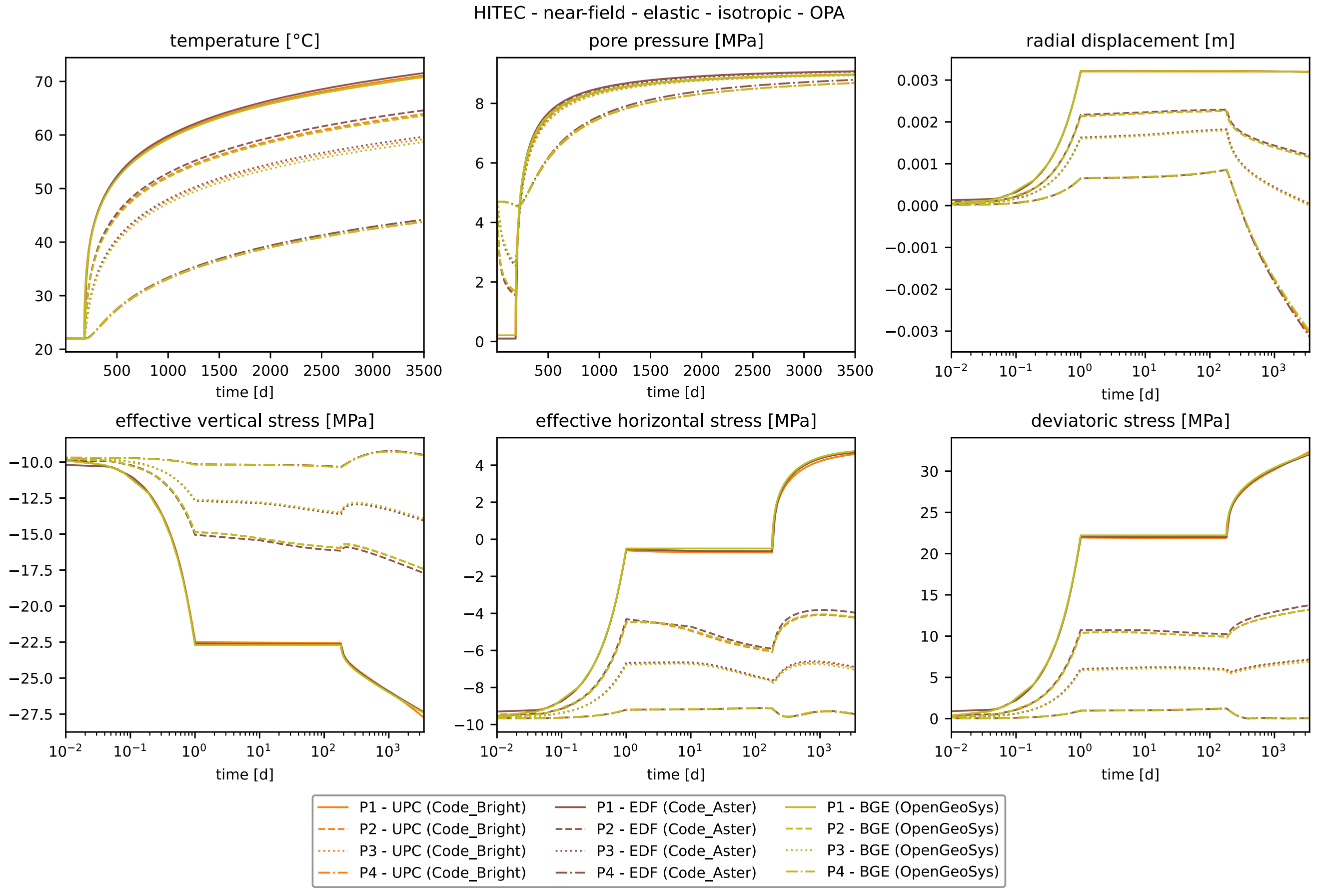

Fig. 8 Benchmark results for the elastic isotropic case in OPA claystone 8

achieved for all variables. The displacement at the observation point P1 obtained by ANDRA with COMSOL Multiphysics deviates a little bit from the rest in the excavation phase. This difference can be explained by the use of a smooth function during the deconfinement phase instead of the use of a linear reduction. Similar to the Boom Clay, the pore pressure evolution is similar at observation points P1, P2, and P3.

The pore pressure increase at P4 is faster and approaches the same asymptotic value of 10.5 MPa as P1, P2, and P3 at the end of the simulation. This indicates that pore pressure becomes homogenized in the surrounding region of the gallery. All teams predict an overpressure in the rock of approximately 5.5 MPa due to the applied heat, compared to the initial conditions. This increase in pore pressure causes tensile stress in the rock, with effective tensile stresses reaching approximately 7.5 MPa at the gallery wall in the horizontal direction. In the vertical direction, the effective stress remains compressive. The tensile stresses decrease with distance from the gallery wall and become negligible at a distance of 0.65 m behind the gallery wall at P2. These results do not necessarily reflect the behaviour of the rock under repository: rock is missing conditions. For a better representation of the repository conditions, the damage of the rock and the resulting permeability increase in the EDZ need to be explicitly taken into account in the modelling. The backfilling of the gallery should also be considered.

7.3 Opalinus claystone: elastic isotropic case

The results of the THM benchmark for Opalinus Clay in the isotropic case are presented in Fig. 8. These results are similar to those of COx discussed in the previous section. BGE, EDF, and UPC participated in this benchmark and their results are in good agreement for all six variables at all observation points.

The higher thermal conductivity of OPA clay compared to COx clay results in lower temperatures, with a maximum of 72 °C at the gallery wall at the end of the simulation, compared to 75 °C for COx clay. There is also a smaller pore overpressure reported during the heating phase for OPA clay, with a maximum value of 8.5 MPa compared to 10.5 MPa for COx clay. This can be explained by the combination of higher permeability and thermal

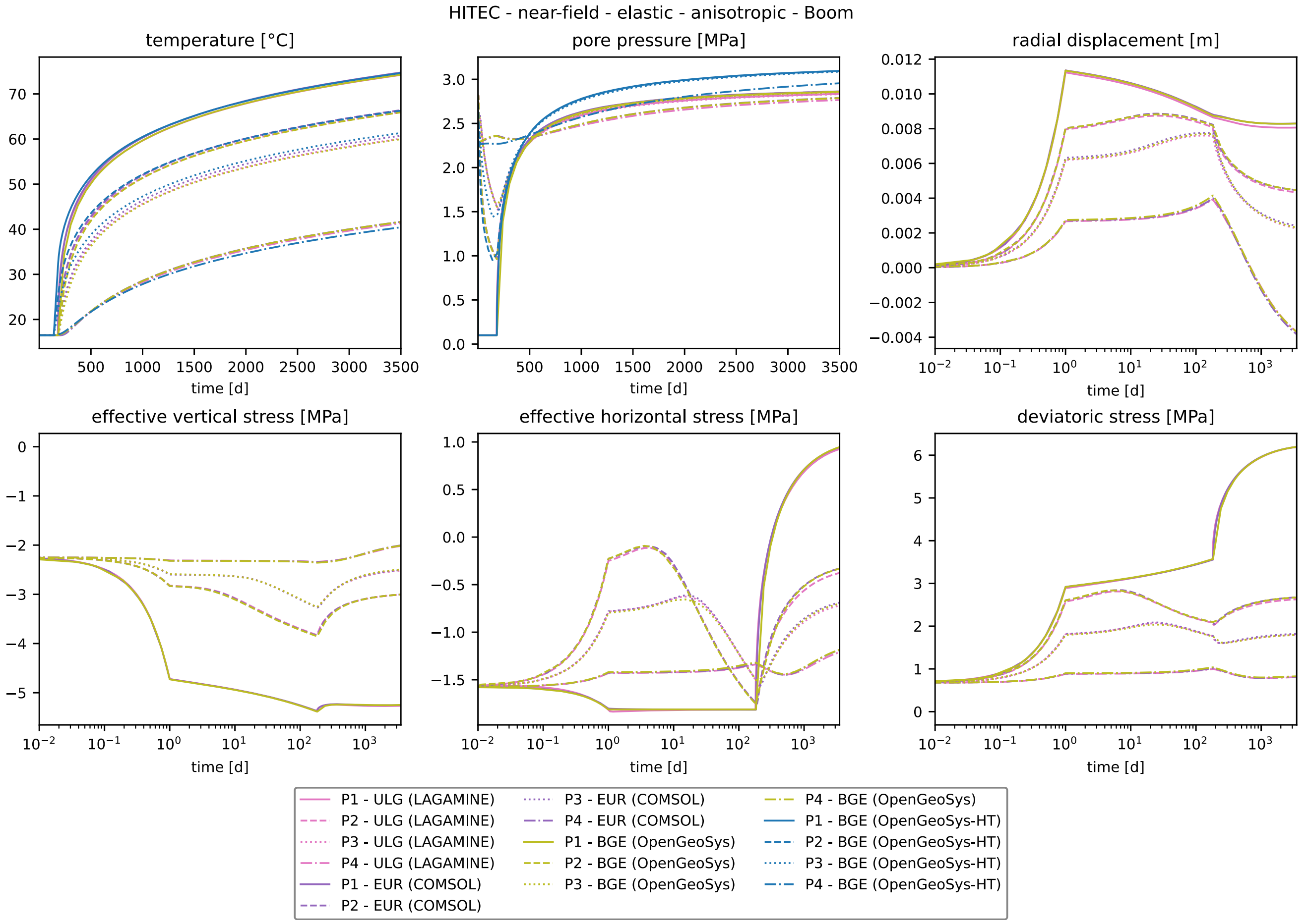

Fig. 9 Benchmark results for the elastic anisotropic case in Boom Clay [8]

expansivity of OPA clay, along with a lower Young's modulus, which allows for pore pressure dissipation and reduces the thermal expansivity contrast between water and the clay matrix. This overpressure causes stress relief, leading to tensile stress at the gallery wall with a maximum value of 4.5 MPa at the end of the simulation. At P2, located 0.65 m behind the wall in the horizontal direction, a compressive stress of more than -4 MPa can be observed at the end of the simulation.

7.4 Boom Clay: elastic anisotropic case

The results of the benchmark simulation for Boom Clay, taking into account anisotropic material properties, are presented in Fig. 9. EUR, ULG and BGE with two process modell participated in this benchmark. In exception of BGE results computed with the hydrothermal model, the results coming from THM process models are consistent for all variables. Pore pressure evolution coming from the hydrothermal model in OpenGeoSys with incorporation of thermo-mechanical effects overestimate the pore overpressure in the heating phase when compared to the results obtained with THM formulations. Further investigations are necessary to adjust this model. Overall, the evolution of pore pressure is similar to the isotropic case, with all pore pressure evolution curves converging towards a value of 2.8 MPa at the end of the simulation. Regarding the mechanical variables, good consistency has been obtained for the displacement and stress results. Multiple iterations were required to achieve a good consistency in this benchmark case. Discrepancies arose in the early stages from ambiguities in the benchmark specifications regarding the anisotropic Poisson ratios. It's important to note that $nu_{ij} \neq nu_{ji}$ for transversely isotropic materials like argillaceous materials. To properly calculate anisotropic components of the Poisson ratios, the orientation of both the numerical model and isotropic plane must be taken into account. Effective communication between teams was key to resolving this issue.

As a result of thermal pressurization, tensile stresses occur at the gallery wall in the horizontal direction. The effective tensile stresses reach a value of nearly 1 MPa at the end of the simulation, which may cause tensile damage

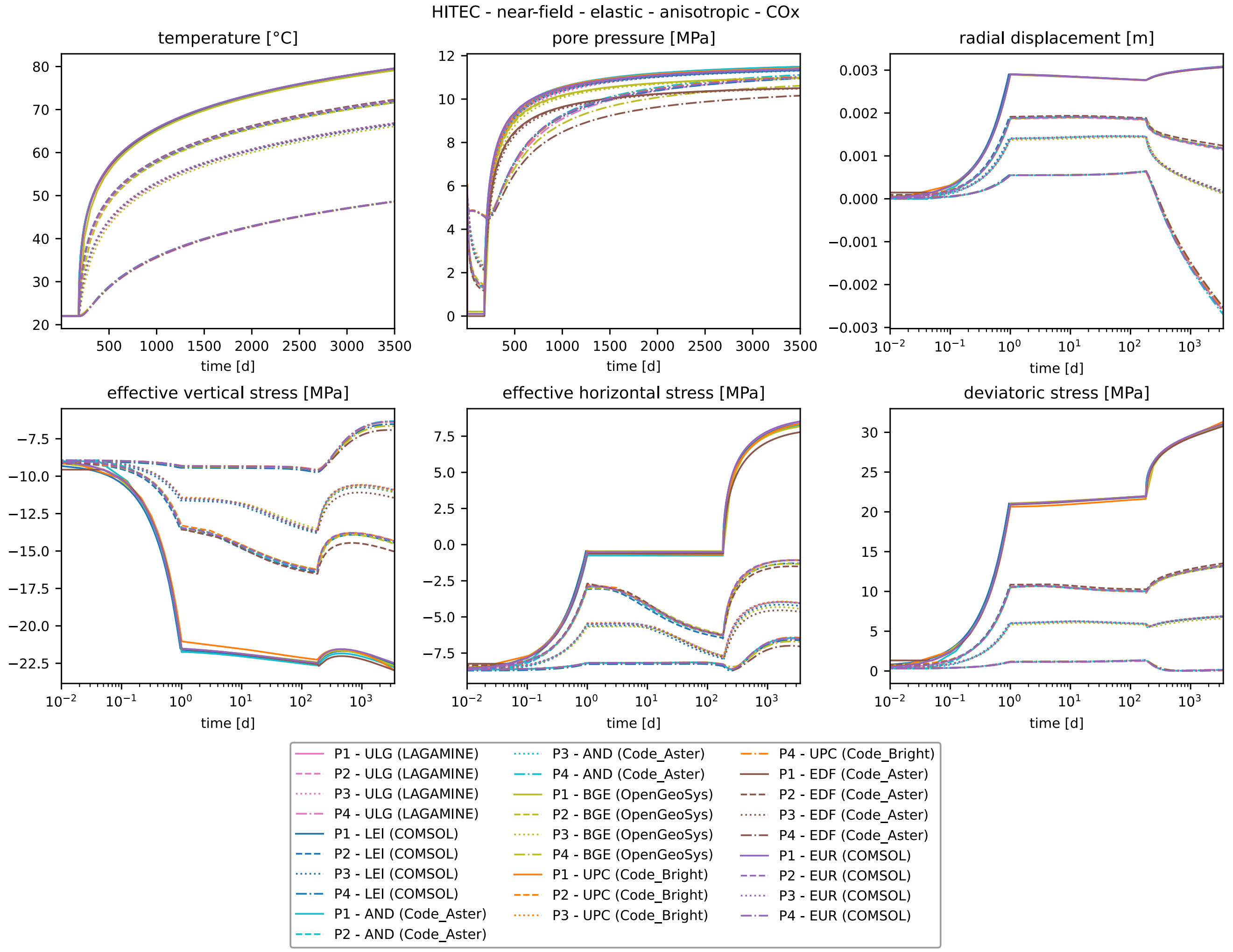

Fig. 10 Benchmark results for the elastic anisotropic case in COx claystone [8]

in the rock if the tensile strength of the rock is exceeded. However, this issue is limited to the boundary because compressive stresses are observed at P2.

7.5 Callovo-Oxfordian claystone: elastic anisotropic case

The results of the subcase 2 for COx clay, assuming anisotropic material properties, are shown in Fig. 10. Seven teams participated in this benchmark (AND, BGE, EDF, EUR, LEI, ULG and UPC), and overall, good agreement has been achieved by all teams. The temperature, displacement and deviatoric stress evolution curves are coincident at all points.

During the heating phase, five teams predicted the same pore pressure evolution trend. Results of BGE and EDF deviate from this trend. The reason for this discrepancy has not yet been found, but differences in the anisotropic Poisson ratios used by these two teams are suspected. The evolution of the effective vertical and horizontal stresses shows small discrepancies at each observation points that can be related to the difference in mesh size and element formulation. This will be further elaborated in the discussion section.

The anisotropy of the COx clay appears to amplify the thermally induced pore pressure, as a maximum value of about 11 MPa was observed in the anisotropic case, compared to about 10 MPa in the isotropic case. The effective horizontal stresses reach approximately 7.5 MPa at the gallery wall, decreasing to less than -1 MPa at P2, which is located 0.65 m behind the gallery wall. At P4, which is located 0.5 m behind the gallery wall, the effect of thermal pressurization is lowest.

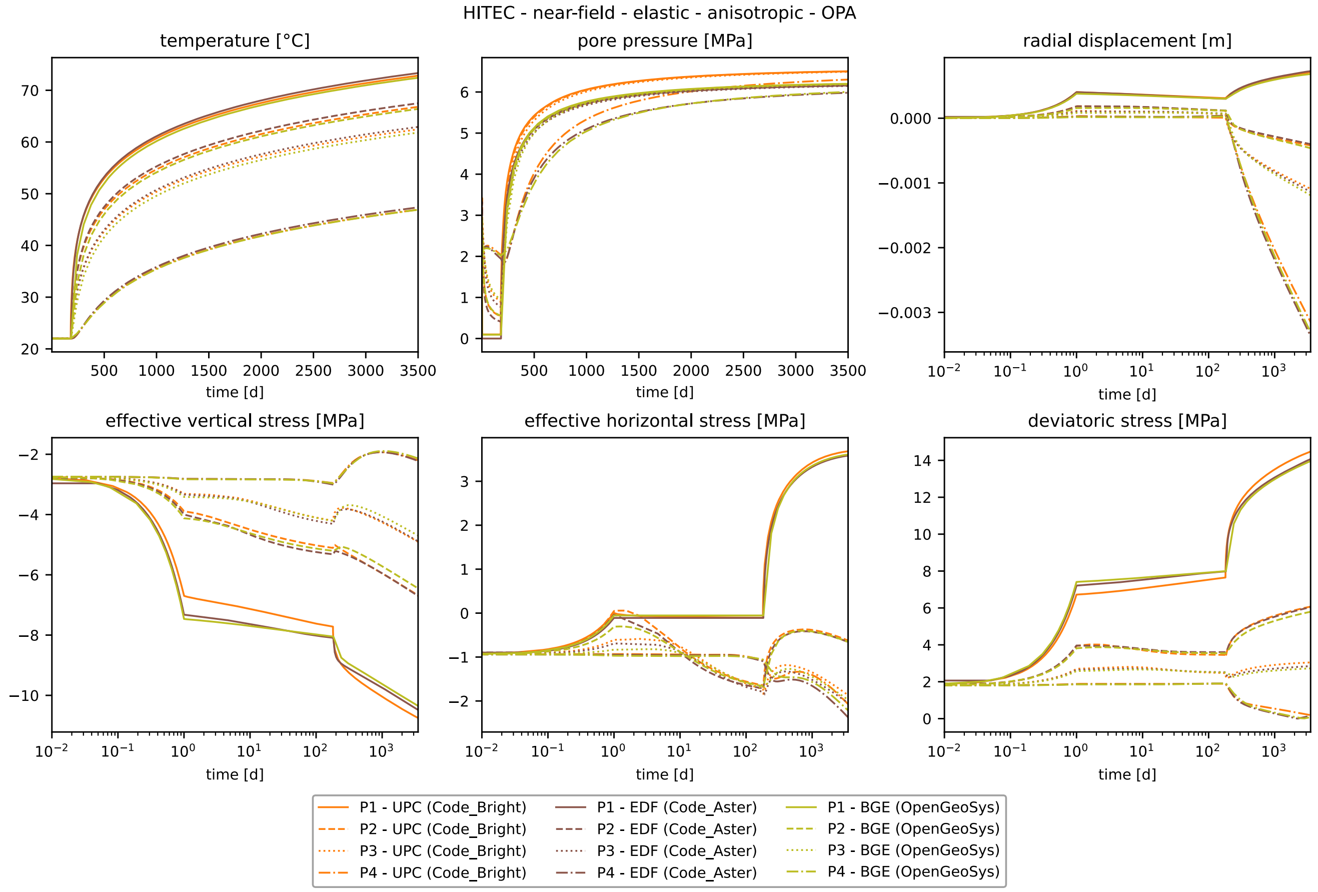

Fig. 11 Benchmark results for the elastic anisotropic case in OPA claystone [8]

7.6 Opalinus claystone: elastic anisotropic case

The results of the final benchmark for Opalinus Clay, taking into account anisotropic material properties, are presented in Fig. 11. The same teams that worked on the isotropic case for Opalinus Clay also participated in this benchmark. The overall results from all teams are in good agreement, with consistent predictions for temperature evolution. UPC predicted the highest pore pressure evolution in this benchmark. EDF and BGE obtained almost identical pore pressure evolution results. In contrast to COx, the results for the anisotropic case in Opalinus Clay show that less overpressure is generated compared to the isotropic case. A maximum overpressure value of about 6 MPa was obtained in this benchmark, while the isotropic case had a maximum value of 8.5 MPa. This may be explained by the higher permeability and higher Poisson ratio in the horizontal direction of the anisotropic Opalinus Clay.

For Opalinus Clay under anisotropic conditions, the displacement results show that the surrounding region moves away from the gallery wall due to thermal expansion in the heating phase. This can be observed at P2, P3 and P4, with P4, located 6.5 m deep in the rock, moving 3 mm away from the gallery wall at the end of the simulation. The effective stress evolution resulting from the pore overpressure shows tensile stresses at the boundary of the gallery wall at P1, which vanish at P2. This effect has been observed in all benchmarks and has been discussed already in previous sections. The comparative assessment of all stress results is in good agreement for all teams except for observation point P1 where UPC predict less effective vertical and deviatoric stresses during the waiting phase.

8 Discussion

Overall, the results of the benchmark studies conducted by the various teams involved showed a high level of consistency in the thermo-hydro-mechanical response of the clay-based materials being studied. These results were more consistent in the isotropic cases, wheareas some discrepancies were observed in the anisotropic benchmarks. In the anisotropic cases, the assumptions taken for

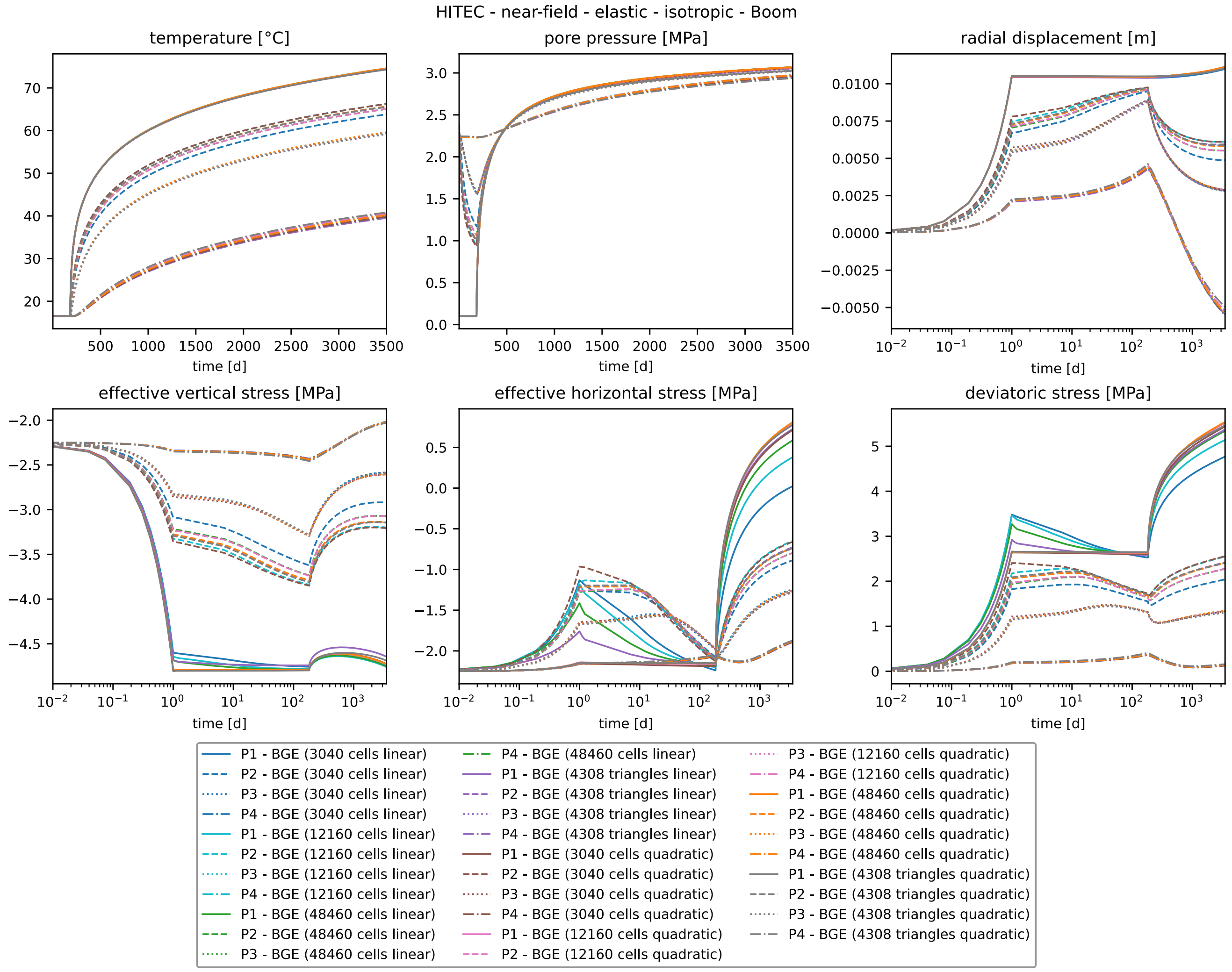

Fig. 12 Comparison of the THM response in OPA at the same distances from the gallery wall parallel (P2, P3) and perpendicular to bedding (P7, P8) based on UPC results

computing the anisotropic components of the Poisson ratios in respect to the coordinate systems used in the different codes have a huge effect on the outcome of the benchmark. There are responsible for the discrepancies in the pore pressure evolution. This can be avoided if the Poisson's ratios are consistently defined in all codes. Other differences in the results obtained by the different teams may be due to a variety of factors, including differences in the governing equations and different solution schemes and codes used, and differences in the numerical meshes employed. A more mathematical investigation is needed to quantify the effect of these factors. This is tedious to perform as much assumptions in this regard are not published and some numerical codes used in this study are not open source.

To better understand the effect of the mesh size and element formulation on the obtained results, a mesh sensitivity study has been performed. Eight different meshes were developed in this study that can be divided into two groups. The first group consists of linear meshes whereas the second group is made of quadratic counterparts derived from the linear meshes. In each group, three meshes were made of quadrilateral elements. The second mesh is derived from the first one with 3040 elements by dividing each element by four to obtain 12160 elements. The third mesh is generated in the same manner by dividing each element of the second mesh by four to obtain 48460 elements. The fourth mesh has been generated using triangular elements. All these meshes were employed to carry out the isotropic benchmark for Boom Clay using OpenGeoSys by BGE. The results of this study are shown in Fig. 12. For all variables, a mesh dependency on the results is observed especially at the observation point P2 where the gradients are highest. The discrepancy in the pore pressure results is observed during the excavation (until 1d) and waiting phase (until 6 months) whereas in the heating phase results

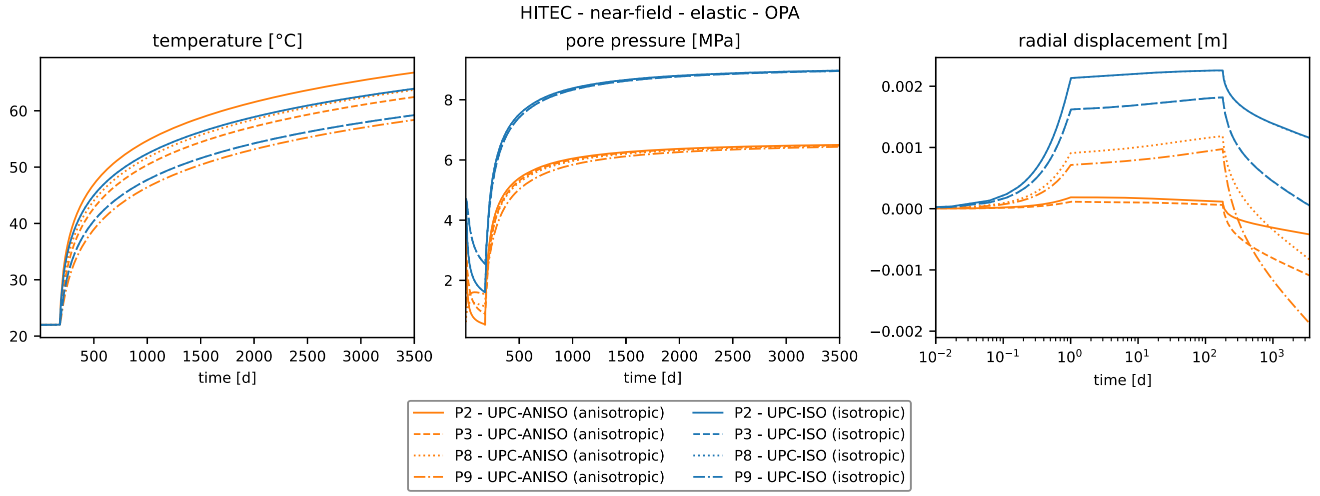

Fig. 13 Comparison of the THM response in OPA at the same distances from the gallery wall parallel (P2, P3) and perpendicular to bedding (P7, P8) based on UPC results

from all meshes are identical. In the excavation phase, some oscillations are observed for all quadrilateral meshes with linear shape functions. This is also the case of the quadratic mesh with 3040 quadrilateral cells. It is important to notice that results with triangular meshes do not show this artefact. Thus, triangular element formulation seems to be more robust for THM simulation at least in OpenGeoSys. This needs to be tested for other codes. The stress evolution curves shows also some scattering of results at observation point P1 for all linear meshes. This is probably the result of the extrapolation problem due to the high gradients near the gallery wall that has been noticed by ULG for the anisotropic cases for Boom Clay and COx in combination with the low approximation order of the derived quantity stress. ULG results for these anisotropic cases at P1 presented in this work have been extrapolated from the integration point to the gallery wall to avoid this issue. The fact that the meshes of the second group do not show this problem further supports this hypothesis. The additional integration points coming with the quadratic elements and the higher approximation order of the stresses help to increase the quality of the extrapolation of the results to the boundary wall.

Based on this study, one can conclude that the discrepancy observed in the benchmark results may be partly explained by the different meshes and element formulations employed by the teams. This is especially the case for results scattering observed near the gallery at P2 and to a smaller extent at P3 as one can be observed for instance in the results of the anisotropic benchmark cases, see for example Fig. 10. Figure 12 shows also that the results of the pore pressure evolution are consistent for all the meshes in the heating phase. Thus the discrepancy observed in the pore pressure results cannot be explained by its dependency on the spatial discretization. The replication of this study based on an anisotropic benchmark case may be necessary to confirm these conclusions. Further analyses may be needed to understand the other underlying mechanisms leading to the discrepancies. However, it can be concluded at this stage that all of the teams involved in this study were able to accurately model the THM evolution of heat-generating repository systems in clay formations and that the tools and techniques they used can be considered verified in this context based on their ability to produce similar results.

The anisotropic effects observed in the benchmark studies were more pronounced in the temperature evolution and mechanical response of the clay-based materials but were not evident in the pore pressure evolution. Instead, the pore pressure appeared to homogenize during the heating phase, reaching similar asymptotic values at the various observation points. This suggests that the anisotropic effects may have a greater influence on the temperature and mechanical behaviour of the materials, but not on the pore pressure, see compare P2 vs. P8 and P3 vs. P9 in Fig. 13. For the isotropic case, the results at the points situated at the same distance from the gallery wall are identical as shown in Fig. 13.

According to the benchmark studies, an increase in pressure was observed during the heating phase in all cases. This phenomenon, known as thermal pressurization, occurs due to the difference in the thermal expansion of water and the clay matrix. The water is constrained by the less expansive clay matrix, leading to an accumulation of pressure. The resulting tensile stresses that may occur in the clay formation as a result of thermal pressurization were observed to be local and to vanish quickly with depth in the rock in the studied benchmarks. However, it is important to note that these results will not be the same in a typical repository configuration with backfilled galleries and multiple canisters disposed of adjacent to one another. Despite this, the results suggest that these tensile stresses may remain local even in this benchmark case and may disappear over time as the thermal power of the radioactive waste decays and the pore pressure decreases. Depending on the tensile strength of the clay, tensile stresses may cause local damage to the clay.

Thermo-hydro-mechanical (THM) simulations can be time-consuming and computationally demanding, particularly when used to assess the safety of repository systems that require the consideration of large geological formations in the numerical analysis. In these cases, the use of numerically efficient methods may be essential to handle the computational demands of such simulations. The TH model with thermo-mechanical storage coefficients proposed by [5] and implemented in the OpenGeoSys has been shown to be able to adequately reproduce the pore overpressure for the isotropic benchmark in Boom Clay. The model slightly overpredicted the thermal induced pore pressure response in the anisotropic case. Further work is necessary to improve the model predictions in such situation. Nevertheless, this model has been found to result in a significant speed-up, up to two orders of magnitude, compared to traditional THM simulations. The actual speed-up depends on the size of the model and the most significant benefits are typically seen in models with a large number of degrees of freedom, where complexity reduction is particularly important. However, for a detailed evaluation of the stress and displacement evolution, fully coupled THM simulations remain necessary [5].

9 Conclusions

The EURAD work package HITEC seeks to enhance the understanding of thermo-hydro-mechanical processes in clay-based materials subjected to elevated temperatures. To this end, a benchmark initiative was conducted to assess the current state of modelling THM phenomena in clay materials. The results of this initiative, which involved teams from across Europe, showed that these teams and their numerical tools are capable of accurately predicting the THM behaviour of clay-based materials such as Boom Clay, Opalinus Clay, and Callovo-Oxfordian clay. In general, the results of the isotropic benchmarks were highly consistent, while some discrepancies were observed in the anisotropic benchmarks, potentially due to differences in the governing equations and codes used, as well as mesh size, element formulations and interpolation algorithms. In conclusion, the results of this benchmark demonstrate the expertise and capabilities of the participating teams in modelling THM phenomena for the safety assessment of repository systems in clay formations. The involved codes can be seen as verified within the framework of “Validation & Verification” (V&V). Further studies that take into account effects of plasticity and permeability changes due to damage are necessary to better reproduce benchmarks at repository conditions. This will be the subject of further publication of the involved teams.

Acknowledgements The project leading to this work has received funding from the European Union’s Horizon 2020 research and innovation programme under grant agreement No. 847593. This paper describes objective technical results and analysis. The authors alone are responsible for the contents of this study.

Author contribution First author wrote the main manuscript. Other authors contributed by providing part related to their numerical analyses.

Funding Open Access funding enabled and organized by Projekt DEAL.

Data availability No datasets were generated or analysed during the current study.

Declarations

Conflict of interest The authors declare no conflict of interest.

References

1. Birkholzer Jens T, Bond Alexander E (2022) DECOVALEX-2019: an international collaboration for advancing the understanding and modeling of coupled thermo-hydro-mechanical-chemical (THMC) processes in geological systems. Int J Rock Mech Min Sci 154(154):105097. https://doi.org/10.1016/j.ijrmms.2022.105097
2. Birkholzer Jens T, Bond Alexander E, Hudson John A, Lanru Jing, Chin-Fu Tsang, Hua Shao, Olaf Kolditz (2018) Decovalex-2015: an international collaboration for advancing the understanding and modeling of coupled thermo-hydro-mechanical-chemical (THMC) processes in geological systems. Environ Earth Sci 77(14):56. https://doi.org/10.1007/s12665-018-7697-7
3. Birkholzer Jens T, Chin-Fu Tsang, Bond Alexander E, Hudson John A, Lanru Jing, Ove Stephansson (2018) 25 years of DECOVALEX-Scientific advances and lessons learned from an international research collaboration in coupled subsurface processes. Int J Rock Mech Min Sci 122:103995. https://doi.org/10.1016/j.ijrmms.2019.03.015
4. Booker JR, Savvidou C (1985) Consolidation around a point heat source. Int J Numer Anal Methods Geomech 9(2):173–184
5. Buchwald J, Kaiser S, Kolditz O, Nagel T (2021) Improved predictions of thermal fluid pressurization in hydro-thermal models based on consistent incorporation of thermo-mechanical effects in anisotropic porous media. Int J Heat Mass Transf 172:121127. https://doi.org/10.1016/j.ijheatmasstransfer.2021.121127
6. Chaudhry AA, Buchwald J, Kolditz O, Nagel T (2019) Consolidation around a point heat source (correction and verification). Int J Numer Anal Methods Geomech 43(18):2743–2751. https://doi.org/10.1002/nag.2998

7. Coussy O (2004) Poromechanics. John Wiley and Sons, Chichester, UK
8. Christophe (Andra) de Lesquen, Minh-ngoc (Andra) Vu, Eric (BGE) Simo, Alexandru (BGE) Tatomir, Paola Léon (BGE) Vargas, Pierre (CNRS-UGrenoble) Bésuelle, Stefano (CNRS-UGrenoble) Dal Pont, Alice (CNRS-UGrenoble) di Donna, Nicolás (CNRS-UGrenoble) Zalamea, Simon (EDF) Raude, Ginger (EDF) El tabbal, Arnaud (EURIDICE) Dizier, Suresh (SCK CEN) Seetharam, Asta (LEI) Narkuniene, Frédéric (ULiège) Collin, Hangbiao (ULiège) Song, Abhishek (ULiège) Rawat, Antonio (UPC) Gens, Fei (UPC) Song HITEC-Deliverable-7.6, Andra, BGE, CNRS-UGrenoble, EDF, EURIDICE, SCK CEN, LEI, ULiège, UPC
9. DDBST (2023) Liquid dynamic viscosity calculation by vogel equation. Dortmund Data Bank Software & Separation Technology (DDBST). URL http://ddbonline.ddbst.de/VogelCalculation/VogelCalculationCGI.exe?component=Water. Accessed 25 Dec 2020
10. Dwivedi D, Arora B, Molins S, Steefel CI (2016) Benchmarking reactive transport codes for subsurface environmental problems. Groundw Assess Model Manag. https://doi.org/10.1201/9781315369044-19
11. Kell George S (1975) Density, thermal expansivity, and compressibility of liquid water from 0. deg. to 150. deg. correlations and tables for atmospheric pressure and saturation reviewed and expressed on 1968 temperature scale. J Chem Eng Data 20(1):97–105. https://doi.org/10.1021/je60064a005
12. Lehmann C, Bilke L, Buchwald J, Graebling N, Grunwald N, Heinze J, Meisel T, Renchao L, Naumov D, Rink K, Sen O, Selzer P, Shao H, Wang W, Zill F, Nagel T, Kolditz O (2024) Openworkflow-development of an open-source synthesis-platform for safety investigations in the site selection process; [openworkflow - entwicklung einer open-source-synthese-plattform für sicherheitsuntersuchungen im standortauswahlverfahren]. Grundwasser 29(1):31–47. https://doi.org/10.1007/s00767-024-00566-9
13. Lux KH, Rutenberg M, Feierabend J, Czaikowski O, Friedenberg L, Maßmann J, Pitz M, Sentis ML, Graupner BJ, Hansmann J, Hotzel S, Kock I, Rutqvist J, Hu M, Rinaldi AP (2023) BenVaSim–International Benchmarking for Verification and Validation of TH2M Simulators with Special Report December 2021, Chair for Waste Disposal Technologies and Geomechanics Clausthal University of Technology
14. Oberkampf William L, Trucano Timothy G, Charles H (2004) Verification, validation, and predictive capability in computational engineering and physics. Appl Mech Rev 57(5):345–384. https://doi.org/10.1115/1.1767847
15. OGS-Community (2024) Saturated point heat source benchmark. 1115https://www.opengeosys.org/docs/benchmarks/th2m/saturatedpointheatsource/. Accessed 11 Sep 2024
16. Pitz M, Kaiser S, Grunwald N, Kumar V, Buchwald J, Wang W, Naumov D, Chaudhry AA, Maßmann J, Thiedau J, Kolditz O, Nagel T (2023) Non-isothermal consolidation: a systematic evaluation of two implementations based on multiphase and Richards equations. Int J Rock Mech Min Sci. https://doi.org/10.1016/j.ijrmms.2023.105534
17. Pardoen B (2015) Hydro-mechanical analysis of the fracturing induced by the excavation of nuclear waste repository galleriesusing shear banding. ULiège - Université de Liège http://reflexions.ulg.ac.be/en/NuclearWasteStorage

Authors and Affiliations

Eric Simo[8,1] · Christophe de Lesquen[2] · Rocio Paola Leon-Vargas[1] · Minh-ngoc Vu[2] · Simon Raude[3] · Ginger El Tabbal[3] · Arnaud Dizier[4] · Suresh Seetharam[4] · Asta Narkuniene[5] · Frédéric Collin[6] · Hangbiao Song[6] · Antonio Gens[7] · Fei Song[7] · Alexandru-Bogdan Tatomir[10] · Thomas Nagel[8,9] · Jörg Buchwald[8,9]

✉ Eric Simo
eric.simo@bge.de

[1] BGE TECHNOLOGY GmbH, Eschenstrasse 55, 31224 Peine, Germany

[2] ANDRA, 1/7 rue Jean Monnet, 92290 Châtenay-Malabry, France

[3] EDF R&D, 7 Bvd Gaspard Monge, 91120 Palaiseau, France

[4] Belgian Nuclear Research Centre (SCK CEN), Boerentang 200, B-2400 Mol, Belgium

[5] Lithuanian Energy Institute, Breslaujos str., 44403 Kaunas, Lithuania

[6] Urban and Environmental Engineering Research Unit, Université de Liège, Allée de la Découverte 9, 4000 Liège, Belgium

[7] Department of Civil and Environmental Engineering, Universitat Politecnica de Catalunya, Jordi Girona 1-3, 08034 Barcelona, Spain

[8] Geotechnical Institute, TU Bergakademie Freiberg, Gustav-Zeuner-Straße 1, 09599 Freiberg, Germany

[9] Helmholtz Centre for Environmental Research-UFZ, Permoserstraße 15, 04318 Leipzig, Germany

[10] BGE mbH, Eschenstrasse 55, 31224 Peine, Germany